

Thermal Hall effect and topological edge states in a square lattice antiferromagnet

Masataka Kawano and Chisa Hotta

Department of Basic Science, University of Tokyo, Meguro-ku, Tokyo 153-8902, Japan

(Dated: February 22, 2019)

We show that the two dimensional spatial inversion-symmetry (SIS) broken square lattice antiferromagnet with easy-plane spin anisotropy exhibits a thermal Hall effect and the edge modes characterized by the \mathbb{Z}_2 topological invariant. These topological properties require a nonzero Berry curvature, and its origin is ascribed to the Dzyaloshinskii-Moriya (DM) interactions or the noncoplanar magnetic ordering generating a U(1) gauge field that couples to the kinetic motion of magnons. Although this picture is established in ferromagnets on the kagome and pyrochlore lattices, it does not apply to our square lattice model since such gauge field cancels out in an edge shared geometry. Instead, our case has an analogy with the anomalous Hall effect of Rashba electronic system where the spin orbit coupling generates an SU(2) gauge field. The two species of magnons defined on antiferromagnetic sublattices can be regarded as the pseudo-spin degrees of freedom of magnons. The DM interactions that emerge due to the SIS breaking serve as a pseudo-spin orbit coupling of magnons and generate a Berry curvature, when the direction of the magnetic moments is properly controlled by the magnetic field. The thermal Hall conductivity of our antiferromagnet shows rapid growth in temperature T beyond the power-law, reflecting the almost gapless low energy branch of the antiferromagnet, which distinctively differs from the $T^{7/2}$ -dependence in the pyrochlore ferromagnets. The present system serves as a standard model for the noncentrosymmetric crystals $\text{Ba}_2\text{MnGe}_2\text{O}_7$ and $\text{Ba}_2\text{CoGe}_2\text{O}_7$.

I. INTRODUCTION

Transport phenomena in insulating magnets are intensively pursued these days, since it turned out that the magnons, quasi-particles of insulating magnets, behave quite similar to the electrons in semiconductors and exhibit a thermal Hall effect¹, a magnon spin Nernst effect^{2–4}, and a magnon-driven spin Seebeck effect⁵. In the typical magnetically ordered insulating states, the low energy collective excitation is well-described by the one-body picture of magnon. Unlike the electron, the magnon is a charge-neutral quasiparticle which does not feel a Lorentz force. Instead, the magnon can feel a Berry curvature, which is a fictitious magnetic field in momentum space. Accordingly, when driven by a temperature gradient, magnons acquire an anomalous velocity and exhibit a thermal Hall effect^{6–35}. A nonzero Berry curvature often indicates the topological nature of magnons represented by the protected edge modes and Chern numbers, which is found in kagome^{12,19,37–43}, pyrochlore^{44–47}, and honeycomb lattices^{22–29,48–54}.

In the previous studies on magnon thermal Hall effects, there always exists an effective U(1) gauge field that couples to magnons and gives a finite Berry curvature. Two main mechanisms to generate such gauge field are proposed. One is to have a noncoplanar magnetic order, on which the magnons hop around, feel the curved spin space and acquire a phase^{12–15}. The other is to make use of an antisymmetric exchange, $\mathbf{D}_{ij} \cdot [\mathbf{S}_i \times \mathbf{S}_j]$, between spins, \mathbf{S}_i and \mathbf{S}_j , called Dzyaloshinskii-Moriya (DM) interaction^{55,56}, which is finite for bonds that have no inversion center. In ferromagnets realized in centrosymmetric crystals, the DM vector \mathbf{D}_{ij} aligned in a staggered manner along the bonds [see Fig.1(a)] gives a Peierls phase, i.e., a U(1) gauge field, to the hopping of

magnons. This happens only when the ordered moments point in the direction *parallel or antiparallel* to the \mathbf{D}_{ij} vectors, which can be controlled by the spin anisotropy and the magnetic field.

However, the presence of DM interaction or a noncoplanar ordering alone is not a sufficient condition to have a finite Berry curvature. Indeed, Refs.[7] and [8] show that the *no-go* condition to have a finite Berry curvature is to have the edge shared lattice geometry, whose symmetry combined with the time reversal symmetry cancels out the effect of U(1) gauge field^{7,8}. The particular choices of lattices that are exempt from this no-go condition are the corner shared kagome^{7,8,12,15–20} and pyrochlore^{6,7,21} lattices, and also the Haldane-type honeycomb lattice^{22–31} with a staggered magnetic field.

The above mentioned mechanism is discussed in a series of centrosymmetric materials having spatial inversion symmetry (SIS), from which the square lattice systems were excluded as *no-go* examples⁵⁷. We show that for the *noncentrosymmetric* square lattice antiferromagnets, the thermal Hall effect and the topologically protected edge modes can emerge from a different mechanism.

In the electronic systems, the anomalous Hall effect is found in the *noncentrosymmetric* materials^{58–65}. Due to the SIS breaking, the Rashba or Dresselhaus spin orbit coupling appears depending on the crystal symmetry^{66–69}. This interaction generates an SU(2) gauge field⁷⁰ that couples the flipping of spins with the antisymmetric right and left propagations of electrons, and generates a finite Berry curvature when the time reversal symmetry (TRS) of the Hamiltonian is broken.

This kind of phenomenon is not observed in ferromagnetic insulators since the magnons carry spins that point in the unique direction and do not host up and down spin degrees of freedom like electrons. In contrast, in antiferromagnets, there are two magnetic sublattices and

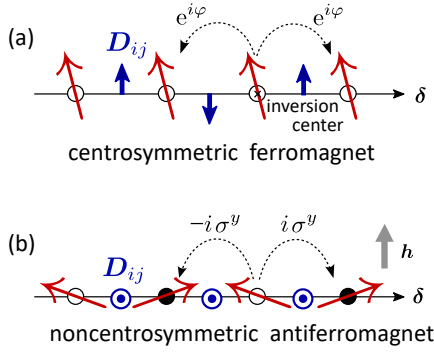


FIG. 1. Schematic illustration of (a) ferromagnet with SIS and (b) antiferromagnet without SIS. The DM vector \mathbf{D}_{ij} is defined by taking the $i \rightarrow j$ in the δ -direction. In (a) the DM vectors align in a staggered manner to keep the SIS, and the hopping of a magnon carry a $U(1)$ gauge field or Peierls phase, φ , which is known to generate a finite Berry curvature. In (b) when a magnon hops to its neighbor it virtually flips the pseudo-spin (since the magnons on different sublattices carry opposite spins) via $i\sigma_y$. Due to the SIS breaking, the sign of hopping to the left and right differs, and together with $i\sigma_y$ generates a finite Berry curvature, which is our main proposal.

accordingly, the two species of magnons are defined on these sublattices, which are regarded as pseudo-spin degrees of freedom. We show that when there exists a set of DM vectors that align uniformly along the bonds due to the SIS breaking, they serve as a pseudo-spin orbit coupling of magnons, and generate a finite Berry curvature. To activate such effect, one needs to control the direction of the magnetic moments as shown in Fig. 1(b) by using the spin anisotropy effect and an external magnetic field; the antiferromagnetic moments must be placed in the plane *perpendicular* to the DM vectors and needs to be canted.

The comparison of Figs.1(a) and 1(b) highlights the difference between the previously studied ferromagnets and our antiferromagnet. In the ferromagnets, the DM vectors are activated when they are *parallel* to the ordered moments, which is exclusive to our case with DM vectors *perpendicular* to the moments. Therefore, the no-go theorem discussed in the ferromagnets that forbids the thermal Hall effect of magnons in the square lattice does not apply to our case. The details will be discussed in §. II C and in §.IV.

The paper is organized as follows; in §.II, we consider the model of two dimensional (2D) SIS broken antiferromagnet, and the conditions to have a Berry curvature. In §.III we demonstrate that the system hosts a thermal Hall effect and \mathbb{Z}_2 topological edge states. In §.IV, we revisit the previous cases of ferromagnets in Fig.1(a) and summarize the no-go condition to clarify the distinct difference from our findings. In §.V, we summarize our results. Our model has correspondence with noncentrosymmetric antiferromagnets $\text{Ba}_2\text{MnGe}_2\text{O}_7$ ⁷¹⁻⁷³ and $\text{Ba}_2\text{CoGe}_2\text{O}_7$ ⁷³⁻⁷⁵, as will be discussed in more detail in the next section.

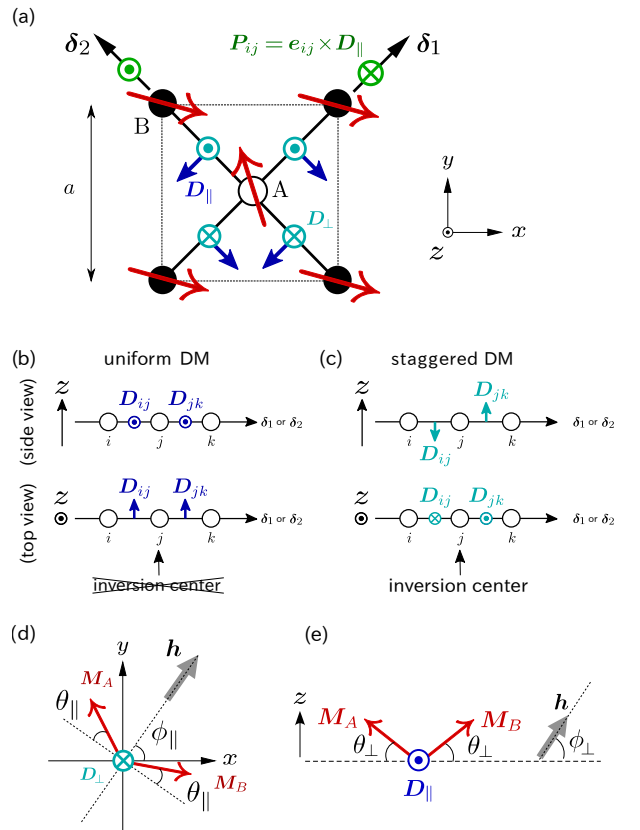


FIG. 2. 2D antiferromagnet with an easy-plane anisotropy, described in Eq.(1). (a) Magnetic unit cell in the easy xy -plane. Open and filled circles represent the A and B magnetic sublattices, respectively, and red arrows are the examples of the classical spin configuration in the ground state. The DM vector, \mathbf{D}_{ij} , has the in-plane (D_{\parallel}) and out-of-plane(D_{\perp}) elements. Here, $(i \rightarrow j)$ is taken in the δ_1 and δ_2 -directions of bonds. The green marks pointing perpendicular to the plane are the polarization vector, $\mathbf{P}_{ij} = \mathbf{e}_{ij} \times \mathbf{D}_{\parallel}$. (b) Uniform and (c) Staggered DM interactions, where only the former breaks the SIS. The directions of the DM vectors are depicted by running the indices in the δ_1 - or δ_2 -directions. (d) The angle of the external magnetic field \mathbf{h} and (e) the canted angle of the magnetic moments against the direction perpendicular to \mathbf{h} .

II. FORMULATION

A. Model

We now consider the 2D square lattice antiferromagnet consisting of N spins, whose Hamiltonian reads

$$\mathcal{H} = J \sum_{\langle i,j \rangle} \mathbf{S}_i \cdot \mathbf{S}_j + \sum_{\langle i,j \rangle} \mathbf{D}_{ij} \cdot [\mathbf{S}_i \times \mathbf{S}_j] + \Lambda \sum_i (S_i^z)^2 - \sum_i \mathbf{S}_i \cdot \mathbf{h}, \quad (1)$$

where $\Lambda > 0$ indicates the uniaxial easy-plane magnetic anisotropy, and \mathbf{D}_{ij} is the DM vector defined on the bond

connecting the i th and j th spins. The magnetic field \mathbf{h} works as a Zeeman term.

Figure 2(a) shows the magnetic unit cell of our square lattice where open and filled circles represent the A- and B-sublattices, respectively. Here, we take the xy -axes in the direction rotated by $\pi/4$ from the bond direction for later convenience. We define two different vectors, $\boldsymbol{\delta}_1 = (\mathbf{e}_x + \mathbf{e}_y)a/2$ and $\boldsymbol{\delta}_2 = (-\mathbf{e}_x + \mathbf{e}_y)a/2$, along the bonds of the square lattice, where we take the length of the unit cell as $a = 1$.

The DM vector has the in-plane and out-of-plane components, \mathbf{D}_{\parallel} and \mathbf{D}_{\perp} , which keep the \bar{C}_4 symmetry of the lattice. \mathbf{D}_{\parallel} is allowed by the Moriya's rule in the D_{2d} or T_d point group symmetry of the crystal, which has relevance to the semiconductors with Dresselhaus type spin orbit interaction⁶⁹. Figure 2(a) shows the \mathbf{D}_{ij} -vectors whose indices $i \rightarrow j$ run in the $\boldsymbol{\delta}_1$ - and $\boldsymbol{\delta}_2$ -directions.

There are two different ways of aligning the DM vector, as shown in Figs. 2(b) and 2(c). The former breaks the SIS and is called the uniform DM interaction. The latter staggered DM interaction does not contribute to the SIS breaking of the lattice. This can be understood simply as follows; When taking site j as an inversion center, the inversion operation exchanges $\mathbf{S}_i \leftrightarrow \mathbf{S}_k$. Therefore, the following part of the Hamiltonian transforms as

$$\begin{aligned} \mathbf{D}_{ij} \cdot [\mathbf{S}_i \times \mathbf{S}_j] + \mathbf{D}_{jk} \cdot [\mathbf{S}_j \times \mathbf{S}_k] \\ \rightarrow -\mathbf{D}_{jk} \cdot [\mathbf{S}_i \times \mathbf{S}_j] - \mathbf{D}_{ij} \cdot [\mathbf{S}_j \times \mathbf{S}_k]. \end{aligned} \quad (2)$$

This straightforwardly indicates that the inversion symmetry is represented by $\mathbf{D}_{ij} = -\mathbf{D}_{jk}$, which holds only in the staggered case [Fig.2(c)]. In our case, \mathbf{D}_{\parallel} is a uniform DM interaction and \mathbf{D}_{\perp} is a staggered DM interaction. We see shortly that even though we include \mathbf{D}_{\perp} in the present model, it does not play any dominant role.

It is convenient to introduce a polarization vector, $\mathbf{P}_{ij} = \mathbf{e}_{ij} \times \mathbf{D}_{\parallel}$, to classify the spatial alignment of \mathbf{D}_{ij} vectors, where \mathbf{e}_{ij} points to either $\boldsymbol{\delta}_1$ or $\boldsymbol{\delta}_2$. The \mathbf{P}_{ij} along $\boldsymbol{\delta}_1$ and $\boldsymbol{\delta}_2$ point in the opposite direction, which we call the *Dresselhaus type DM interaction*. One can define another model by converting \mathbf{D}_{\parallel} along the $\boldsymbol{\delta}_2$ -direction up side down⁷⁶. In this case, all the \mathbf{P}_{ij} 's are in the $-z$ direction, which we call the *Rashba type DM interaction*, since it shares the same geometry with the Rashba spin orbit coupling generated by the electric field perpendicular to the plane⁶⁶⁻⁶⁸. Since the two types of geometry only change the sign of the Hall conductivity, we focus on the Dresselhaus type in the present paper. The mechanism to realize a nonvanishing Berry curvature is the same for both types.

The Hamiltonian Eq.(1) serves as a standard model for $\text{Ba}_2\text{MnGe}_2\text{O}_7$ and $\text{Ba}_2\text{CoGe}_2\text{O}_7$ with space group $P\bar{4}2_1m$ ⁷³. The MnO_4 or CoO_4 tetrahedra form a square lattice, which has an easy-plane anisotropy. The slightly canted antiferromagnetic order is realized in the easy-plane below 4K in $\text{Ba}_2\text{MnGe}_2\text{O}_7$ ⁷¹ and below 7K in $\text{Ba}_2\text{CoGe}_2\text{O}_7$ ⁷⁴. The canting is induced by the out-of-plane components of the DM interaction, \mathbf{D}_{\perp} . The mag-

netic anisotropy inside the easy-plane is tiny in both materials and can be neglected. The Dresselhaus type DM interaction, \mathbf{D}_{\parallel} , is compatible with the crystal symmetry of these materials and should be present, although its amplitude is not clarified.

For later convenience, we decompose the magnetic field, \mathbf{h} , into the ones parallel and perpendicular to the easy-plane as, $\mathbf{h} = \mathbf{h}_{\parallel} + \mathbf{h}_{\perp}$. The in-plane magnetic field, \mathbf{h}_{\parallel} , fixes the in-plane direction of the magnetic moments [Fig.2(d)]. The out-of-plane magnetic field, \mathbf{h}_{\perp} , cant the spins off the plane, as shown in Fig.2(e). The angles of these moments are described by the field angle about the Cartesian coordinates, ϕ_{\parallel} and ϕ_{\perp} , as well as by the canting angles, θ_{\parallel} and θ_{\perp} , against the axes perpendicular to \mathbf{h} .

B. Spin-wave analysis

In the following, we apply a spin-wave analysis to Eq.(1). For sufficiently small D_{\parallel} compared to Λ , the canted antiferromagnetic order is realized (see Appendix A), whose angles θ_{\parallel} and θ_{\perp} are determined numerically by minimizing the classical energy,

$$\begin{aligned} E(\theta_{\parallel}, \theta_{\perp}) = & -2JNS^2(\cos 2\theta_{\parallel} \cos^2 \theta_{\perp} - \sin^2 \theta_{\perp}) \\ & - 2D_{\perp}NS^2 \sin 2\theta_{\parallel} \cos^2 \theta_{\perp} + \Lambda NS^2 \sin^2 \theta_{\perp} \\ & - hNS(\sin \phi_{\perp} \sin \theta_{\perp} + \cos \phi_{\perp} \sin \theta_{\parallel} \cos \theta_{\perp}). \end{aligned} \quad (3)$$

Before applying the Holstein-Primakoff transformation, we need to set the z -axis of each spin independently to these directions by the local unitary transformation⁷⁷, $U^{\dagger} \mathcal{H} U$, with U given as,

$$\begin{aligned} U = & \exp\left(i \sum_j \frac{\pi}{2} S_j^x\right) \exp\left(-i \sum_j (\theta_{\parallel} e^{i\mathbf{Q} \cdot \mathbf{r}_j} - \phi_{\parallel}) S_j^y\right) \\ & \times \exp\left(-i \sum_j \theta_{\perp} e^{i\mathbf{Q} \cdot \mathbf{r}_j} S_j^x\right), \end{aligned} \quad (4)$$

where, \mathbf{r}_j , is the spatial coordinate of site- j , and \mathbf{Q} is the ordering wave vector which satisfy $e^{i\mathbf{Q} \cdot \mathbf{r}_j} = \pm 1$ for sublattices A and B, respectively. The transformed spin operators are antiparallel, and are given by the standard Holstein-Primakoff transformation⁷⁸ for the two magnetic sublattices, A and B as,

$$S_i^+ \simeq \sqrt{2S} a_i \quad S_i^- \simeq \sqrt{2S} a_i^{\dagger} \quad S_i^z = S - a_i^{\dagger} a_i, \quad (5)$$

and

$$S_j^+ \simeq \sqrt{2S} b_j^{\dagger} \quad S_j^- \simeq \sqrt{2S} b_j \quad S_j^z = -S + b_j^{\dagger} b_j, \quad (6)$$

respectively. After a Fourier transformation, $a_i = \sqrt{2/N} \sum_{\mathbf{k}} a_{\mathbf{k}} e^{i\mathbf{k} \cdot \mathbf{r}_i}$ and $b_j = \sqrt{2/N} \sum_{\mathbf{k}} b_{\mathbf{k}} e^{i\mathbf{k} \cdot \mathbf{r}_j}$, we find the bosonic Bogoliubov-de Gennes (BdG) Hamiltonian described in the 4×4 form with a vector $\Phi_{\mathbf{k}} = (a_{\mathbf{k}}, b_{\mathbf{k}}, a_{-\mathbf{k}}^{\dagger}, b_{-\mathbf{k}}^{\dagger})^T$, as

$$U^{\dagger} \mathcal{H} U \simeq \text{const} + \frac{1}{2} \sum_{\mathbf{k}} \Phi_{\mathbf{k}}^{\dagger} H_{\text{BdG}}(\mathbf{k}) \Phi_{\mathbf{k}}, \quad (7)$$

$$H_{\text{BdG}}(\mathbf{k}) = \begin{pmatrix} \Xi_{\mathbf{k}} & \Delta_{\mathbf{k}} \\ \Delta_{-\mathbf{k}}^* & \Xi_{-\mathbf{k}}^* \end{pmatrix}, \quad (8)$$

where $\mathbf{k} = (k_x, k_y)$ is defined on a 2D reciprocal space. $\Xi_{\mathbf{k}}$ and $\Delta_{\mathbf{k}}$ are the 2×2 matrices, and satisfy $\Xi_{\mathbf{k}}^\dagger = \Xi_{\mathbf{k}}$ and $\Delta_{\mathbf{k}}^\dagger = \Delta_{-\mathbf{k}}^*$, respectively. To diagonalize the bosonic BdG Hamiltonian, $H_{\text{BdG}}(\mathbf{k})$, we need to solve the following eigenvalue equation⁷⁹,

$$\Sigma^z H_{\text{BdG}}(\mathbf{k}) \mathbf{t}_\pm(\mathbf{k}) = \omega_\pm(\mathbf{k}) \mathbf{t}_\pm(\mathbf{k}), \quad (9)$$

where $\Sigma^z = \tau^z \otimes \sigma^0$, and τ^μ , σ^μ ($\mu = 0, x, y, z$) are the Pauli matrix (and unit matrix $\mu = 0$) acting on a particle-hole space and a sublattice space, respectively. The magnon bands, $\omega_\pm(\mathbf{k}) \geq 0$, and the corresponding eigenvectors, $\mathbf{t}_\pm(\mathbf{k}) = (u_{\pm,A}(\mathbf{k}), u_{\pm,B}(\mathbf{k}), v_{\pm,A}(\mathbf{k}), v_{\pm,B}(\mathbf{k}))^T$, are obtained, which satisfy the following paraunitary condition,

$$T(\mathbf{k}) = (\mathbf{t}_+(\mathbf{k}) \ \mathbf{t}_-(\mathbf{k}) \ \Sigma^x \mathbf{t}_+^*(-\mathbf{k}) \ \Sigma^x \mathbf{t}_-^*(-\mathbf{k})) , \quad (10)$$

$$T^\dagger(\mathbf{k}) \Sigma^z T(\mathbf{k}) = T(\mathbf{k}) \Sigma^z T^\dagger(\mathbf{k}) = \Sigma^z, \quad (11)$$

where $\Sigma^x = \tau^x \otimes \sigma^0$. The index, \pm , denotes the upper and lower magnon bands, respectively. The analytical form of the magnon bands and the eigenvectors are shown in Appendix. B.

C. Symmetry and Berry curvature

A Berry curvature contributes to the thermal Hall effect and the topological nature of the system, and is defined as¹¹

$$\Omega_{xy}^{(\pm)}(\mathbf{k}) = -2\text{Im} \left[\frac{\partial \mathbf{t}_\pm^\dagger(\mathbf{k})}{\partial k_x} \Sigma^z \frac{\partial \mathbf{t}_\pm(\mathbf{k})}{\partial k_y} \right]. \quad (12)$$

The thermal Hall conductivity is given by the following formula¹¹,

$$\kappa_{xy} = -\frac{k_B^2 T}{\hbar} \int_{\text{BZ}} \frac{d^2 \mathbf{k}}{(2\pi)^2} \sum_{\eta=\pm} \left\{ c_2[f(\omega_\eta(\mathbf{k}))] - \frac{\pi^2}{3} \right\} \Omega_{xy}^{(\eta)}(\mathbf{k}), \quad (13)$$

where $f(\omega) = 1/\{\exp(\omega/k_B T) - 1\}$ is the Bose distribution function, and $c_2[x] = \int_0^x dt [\ln\{(1+t)/t\}]^2$.

The way to understand the condition for a nonvanishing Berry curvature is three-fold. First, we see that the A- and B-sublattices form a pseudo-spin degrees of freedom and breaking its pseudo-TRS and SIS via $\mathbf{D}_{\parallel} \neq 0$ is the necessary condition to have $\Omega_{xy}^{(\pm)}(\mathbf{k}) \neq 0$. Second, we need to properly set the relative angles between adjacent magnetic moments and the DM vector to have a contribution to the magnon excitation from each bond via $\mathbf{D}_{ij} \cdot [\mathbf{S}_i \times \mathbf{S}_j]$. This will require $\mathbf{M}_A, \mathbf{M}_B \perp \mathbf{D}_{\parallel}$ as well as a canting of the magnetic moments by \mathbf{h} . Finally, we need to have $\text{Im}(H_{\text{BdG}}(\mathbf{k})) \neq 0$ after summing up the above contributions from bonds, avoiding the cancellations from the symmetry of the system, which is attained

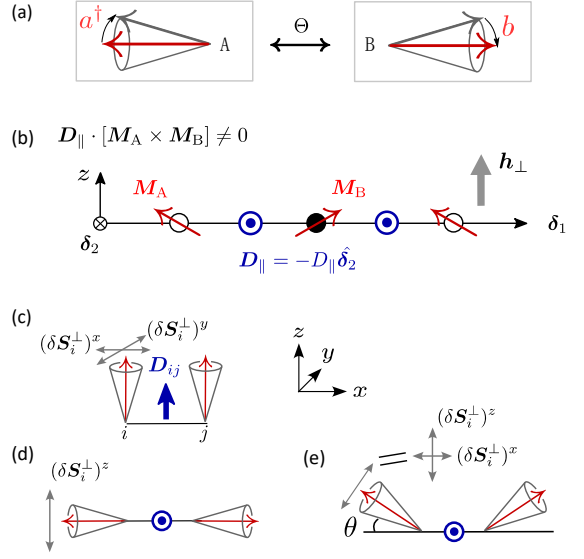


FIG. 3. (a) Sketch of the effective TRS operation in the present system in Eq.(15). (b) Schematic description of the antiferromagnetic state that gives $\Omega_{xy}^{(\pm)}(\mathbf{k}) \neq 0$, extracting the δ_1 -direction from Fig.2(a). When $\mathbf{h}_\perp \neq 0$, the ordered magnetic moment and the uniform DM vector form a finite solid angle. (c)-(e) Schematic illustration of the magnetic moments and DM vector. The DM vector perpendicular to the collinear magnetic moments as in (d) does not contribute the magnon excitation. However, when the spins cant as in (e), the DM vector can couple to the kinetic motion of magnons, and generates a finite Berry curvature.

for the uniform DM vectors in Fig.2(b). Once these three conditions are fulfilled, $\mathbf{D}_{ij} = \mathbf{D}_{\parallel} \neq 0$ serves as a pseudo-spin orbit interaction on magnons, and $\Omega_{xy}^{(\pm)}(\mathbf{k}) \neq 0$ is realized in a similar way to the case of the anomalous Hall effect in Rashba electronic systems.

Often, the symmetry of the system puts some constraints on its Berry curvature. In the electronic systems, the SIS gives $\Omega(-\mathbf{k}) = \Omega(\mathbf{k})$ and TRS gives $\Omega(-\mathbf{k}) = -\Omega(\mathbf{k})$. The combination of SIS and TRS leads to $\Omega(\mathbf{k}) = 0$ for all \mathbf{k} . The similar context holds for magnons. Let us show that if $\mathbf{D}_{\parallel} = \mathbf{0}$, the SIS and TRS in the language of magnons are present, and we find $\Omega_{xy}^{(\pm)}(\mathbf{k}) = 0$. For $\mathbf{D}_{\parallel} = \mathbf{0}$ the bosonic BdG Hamiltonian in Eq.(8) satisfies the following two equations,

$$H_{\text{BdG}}(-\mathbf{k}) = H_{\text{BdG}}(\mathbf{k}), \quad (14)$$

$$\Theta H_{\text{BdG}}(-\mathbf{k}) \Theta^{-1} = H_{\text{BdG}}(\mathbf{k}), \quad (15)$$

where we introduce the anti-unitary operator $\Theta = (\tau^0 \otimes \sigma^x)K$, using the complex conjugation operator K . Equation (14) reflects the SIS of the Hamiltonian. In Eq.(15), the bosonic BdG Hamiltonian is invariant under the symmetry operation represented by Θ . This operator exchanges $a^\dagger \leftrightarrow b$ and $b^\dagger \leftrightarrow a$, namely, the creation of spin moments on A-sublattice is converted to the annihilation of spin moments on B-sublattice pointing in

the opposite direction. Let us regard the antiferromagnetic moments on two sublattices as a spinor degrees of freedom. Then, Θ serves as *an effective time reversal symmetry operator* that flips the spinor upside down, as shown schematically in Fig.3(a). In analogy with the above mentioned electronic systems, the combination of SIS in Eqs.(14) and the pseudo-TRS in (15) straightforwardly gives $\Omega_{xy}^{(\pm)}(\mathbf{k}) = 0$. (See §.IV for the details of the formulation). Therefore, $\mathbf{D}_{\parallel} \neq 0$ is the necessary condition to have a nonvanishing Berry curvature.

To examine the second condition, we decompose \mathbf{S}_i into the ordered moment and the fluctuation part as, $\mathbf{S}_i = \langle \mathbf{S}_i \rangle + \delta \mathbf{S}_i^{\parallel} + \delta \mathbf{S}_i^{\perp}$, where $\delta \mathbf{S}_i^{\parallel} \parallel \langle \mathbf{S}_i \rangle$ and $\delta \mathbf{S}_i^{\perp} \perp \langle \mathbf{S}_i \rangle$. $\delta \mathbf{S}_i^{\perp}$ represents the kinetic motion of magnons. Then, the DM interaction term can be written as,

$$\mathbf{D}_{ij} \cdot [\mathbf{S}_i \times \mathbf{S}_j] \simeq \mathbf{D}_{ij} \cdot [\delta \mathbf{S}_i^{\perp} \times \delta \mathbf{S}_j^{\perp}] + \text{const.} \quad (16)$$

We ignore the on-site terms such as $\mathbf{D}_{ij} \cdot [\delta \mathbf{S}_i^{\parallel} \times \langle \mathbf{S}_j \rangle]$, which do not affect the following discussion. The first term of the right-hand side of Eq. (16) is nonzero only when the fluctuation components of the two spins, $\delta \mathbf{S}_i^{\perp}$ and $\delta \mathbf{S}_j^{\perp}$, are neither parallel nor antiparallel and have components perpendicular to \mathbf{D}_{ij} . This can be easily attained in a typical ferromagnet shown in Fig.3(c), where each spin has the 2D fluctuation $(\delta \mathbf{S}_i^{\perp})^x$ and $(\delta \mathbf{S}_i^{\perp})^y$, that can couple to \mathbf{D}_{ij} parallel to the magnetic moments. In contrast, for the collinear antiferromagnets in Fig.3(d), there is only one element of fluctuation perpendicular to \mathbf{D}_{ij} as $\delta \mathbf{S}_i^{\perp} \simeq \sqrt{S/2}(0, a_i^{\dagger} + a_i, -i(a_i^{\dagger} - a_i))$ and $\delta \mathbf{S}_j^{\perp} \simeq \sqrt{S/2}(0, b_j + b_j^{\dagger}, -i(b_j - b_j^{\dagger}))$, which suppresses the coupling as

$$\mathbf{D}_{ij} \cdot [\delta \mathbf{S}_i^{\perp} \times \delta \mathbf{S}_j^{\perp}] \simeq 0. \quad (17)$$

To activate the coupling, we need to make \mathbf{M}_A and \mathbf{M}_B noncollinear by applying a magnetic field as shown in Fig.3(e), and the x - and z -components of fluctuation emerge from the canting angle $\theta_{\perp} \neq 0$ as

$$\begin{aligned} \delta \mathbf{S}_i^{\perp} &\simeq \sqrt{\frac{S}{2}}(-i(a_i^{\dagger} - a_i)\sin\theta_{\perp}, a_i^{\dagger} + a_i, -i(a_i^{\dagger} - a_i)\cos\theta_{\perp}), \\ \delta \mathbf{S}_j^{\perp} &\simeq \sqrt{\frac{S}{2}}(i(b_j - b_j^{\dagger})\sin\theta_{\perp}, b_j + b_j^{\dagger}, -i(b_j - b_j^{\dagger})\cos\theta_{\perp}) \end{aligned} \quad (18)$$

Then, by setting \mathbf{M}_A and \mathbf{M}_B perpendicular to \mathbf{D}_{ij} we get the maximum contribution as

$$\mathbf{D}_{ij} \cdot [\delta \mathbf{S}_i^{\perp} \times \delta \mathbf{S}_j^{\perp}] \simeq \frac{1}{2} D_{ij} S \sin 2\theta_{\perp} (a_i^{\dagger} b_j - a_i^{\dagger} b_j^{\dagger} + \text{h.c.}) \quad (19)$$

We see shortly that the thermal Hall effect appears only when applying a field and having $\theta_{\perp} \neq 0$.

The final goal is to have a finite imaginary contribution to the BdG Hamiltonian after summing up Eq.(19) throughout the system. If $\text{Im}(H_{\text{BdG}}(\mathbf{k})) = 0$, one can always choose a real eigenvector $\mathbf{t}_{\pm}(k)$, which immediately gives $\Omega_{xy}^{(\pm)}(\mathbf{k}) = 0$ [see Eq.(12)]. Therefore, having a finite imaginary part of $H_{\text{BdG}}(\mathbf{k})$ is necessary for

$\Omega_{xy}^{(\pm)}(\mathbf{k}) \neq 0$. Notice that Fig.3(e) does not generate a U(1) gauge field that gave such imaginary part to the Hamiltonian in ferromagnets, since the coefficient in the right-hand side of Eq.(19) is real. As mentioned, we are considering $\mathbf{D}_{ij} = \mathbf{D}_{\parallel}$ which breaks the SIS, namely the hopping of magnon to left and right lattice sites have different signs as

$$\begin{aligned} &\frac{1}{2} D_{\parallel} S \sin 2\theta_{\perp} (a_j^{\dagger} b_{j+1} + a_j b_{j+1}^{\dagger} - a_j^{\dagger} b_{j-1} + a_j b_{j-1}^{\dagger}) \\ &= i D_{\parallel} \sin 2\theta_{\perp} \sin k a_k^{\dagger} b_k + \text{h.c.} \\ &\propto \psi_k^{\dagger} (\sigma^y \sin k) \psi_k, \end{aligned} \quad (20)$$

where we introduced $\psi_k = (a_k, b_k)^T$ for convenience as a pseudo-spinor operator. Since the hopping converts the a_j -magnons to $b_{j\pm 1}$ -magnons, it accompanies a pseudo-spin flip, and since it is antisymmetric, we find $\pm i \sigma_y$ as we showed in Fig.1(b), which is the origin of $\text{Im}(H_{\text{BdG}}(\mathbf{k})) \neq 0$. This has the same form as the well-known Rashba spin orbit term of the electronic Hamiltonian for which we set $\psi_k = (c_{k\uparrow}, c_{k\downarrow})^T$ with $c_{k\sigma}$ an annihilation operator of electron with spin σ . Note that even when Eq.(19) holds, if the SIS is not broken and the alignment of DM vectors is staggered as in Fig.3(c) the sign of the hopping of the left and right moving magnons is the same and $\text{Im}(H_{\text{BdG}}(\mathbf{k})) = 0$.

To summarize, $\mathbf{D}_{\parallel} \neq 0$ that breaks the SIS serves as an effective Rashba-type spin orbit coupling of the magnons whose two sublattices forms a pseudo spin degrees of freedom. It also breaks the pseudo-TRS, and $\Omega_{xy}^{(\pm)}(\mathbf{k}) \neq 0$ becomes feasible. On the top of that, we need to cant the antiferromagnetic moments off the collinear configuration by the magnetic field, $\mathbf{h}_{\perp} \neq \mathbf{0}$. Then, the following term appears in $H_{\text{BdG}}(\mathbf{k})$,

$$(\tau^0 \otimes \sigma^y - \tau^x \otimes \sigma^y) S \sum_{\mu=1,2} \sum_{\nu \neq \mu} D_{\parallel} \hat{\delta}_{\mu} \cdot [\mathbf{M}_A \times \mathbf{M}_B] \sin \mathbf{k} \cdot \boldsymbol{\delta}_{\nu}, \quad (21)$$

where $\hat{\delta}_{\mu}$ is a unit vector pointing in the $\boldsymbol{\delta}_{\mu}$ -direction ($\mu = 1, 2$). This term is a complex matrix that originates from the solid angle subtended by \mathbf{M}_A , \mathbf{M}_B , and \mathbf{D}_{\parallel} [see Fig.3(b)], and generates a finite Berry curvature.

D. \mathbb{Z}_2 topological invariant

A finite Berry curvature may also imply the emergence of a topological phase. To examine it, we prepare a square shaped lattice by taking a periodic boundary in the $\boldsymbol{\delta}_1$ -directions, extend the $\boldsymbol{\delta}_2$ -direction over $2L$ lattice sites and leave its edges open. The Fourier transform is given only for the periodic boundary condition where the wave number, $k_{\boldsymbol{\delta}_1}$, is well defined. The Hamiltonian yields $2L$ pairs of particle and hole energy bands and we examine whether there are topologically protected edge modes that cross the energy gap.

The existence of the topologically protected edge modes can be explained using the topological invariant.

Our system has a band degeneracy at some points in the Brillouin zone so we cannot straightforwardly define a magnon Chern number as in Ref.[80]. However, a proper choice of the direction of the magnetic field allows the magnon bands to be gapped throughout the Brillouin zone except at the corner, and a winding number is well defined along $\mathbf{k} = \mathbf{k}_{\delta_2}$, parallel to δ_2 .

Practically, the \mathbb{Z}_2 topological invariant of the magnon system in one dimension has not been discussed so far. We thus define it by extending the one for topological superconductors^{81,82}. Using the paraunitary matrix in Eq.(10), we first define a gauge field as

$$\mathbf{A}(\mathbf{k}) = -i\text{Tr}[\Sigma^z T^\dagger(\mathbf{k}) \Sigma^z \nabla_{\mathbf{k}} T(\mathbf{k})]. \quad (22)$$

which is rewritten using $T^{-1}(\mathbf{k}) = \Sigma^z T^\dagger(\mathbf{k}) \Sigma^z$ as

$$\mathbf{A}(\mathbf{k}) = \nabla_{\mathbf{k}} \arg\{\det T(\mathbf{k})\} \quad (23)$$

Then, the winding number at each fixed k_{δ_1} is constructed as

$$\begin{aligned} W(k_{\delta_1}) &= \frac{1}{2} \int_{\text{BZ}(k_{\delta_1})} dk_{\delta_2} A_{\delta_2}(\mathbf{k}) \\ &= \frac{1}{2} \int_{\text{BZ}(k_{\delta_1})} dk_{\delta_2} \frac{\partial}{\partial k_{\delta_2}} \arg\{\det T(\mathbf{k})\}, \end{aligned} \quad (24)$$

where $\text{BZ}(k_{\delta_1})$ is the line over the Brillouin zone at fixed k_{δ_1} . In addition, the following relation holds when $\phi_{\parallel} \neq 0$ ($\text{mod } \pi/2$), $\mathbf{D}_{\parallel} \neq \mathbf{0}$, and $\mathbf{h}_{\perp} \neq \mathbf{0}$:

$$\det T(\pm\pi, q) = \det T(q, \pm\pi) \quad (q \in \partial\text{BZ}), \quad (25)$$

where ∂BZ is the surface of the Brillouin zone. The \mathbb{Z}_2 topological invariant is defined as,

$$\nu(k_{\delta_1}) = e^{iW(k_{\delta_1})}. \quad (26)$$

The value, $\nu(k_{\delta_1}) = -1$, discriminates the \mathbb{Z}_2 topological band structure from the trivial one having $\nu(k_{\delta_1}) = 1$.

When $\mathbf{D}_{\parallel} = \mathbf{0}$, there is always a band degeneracy over the Brillouin zone boundary. Thus, we cannot define the winding number. When $\mathbf{h}_{\perp} = \mathbf{0}$, $H_{\text{BdG}}(\mathbf{k})$ is the real matrix, and the topological invariant is always trivial, $\nu(k_{\delta_1}) = 1$. Thus, one can conclude that $\mathbf{D}_{\parallel} \neq \mathbf{0}$ and $\mathbf{h}_{\perp} \neq \mathbf{0}$ are the necessary conditions to have a feasible $\nu(k_{\delta_1}) = -1$. We will also discuss the ϕ_{\parallel} dependence of a topological invariant in §.III C.

III. RESULTS

A. Berry curvature

Let us demonstrate the emergent Berry curvature and the thermal Hall conductivity in our SIS broken square lattice antiferromagnet. The Berry curvature is activated

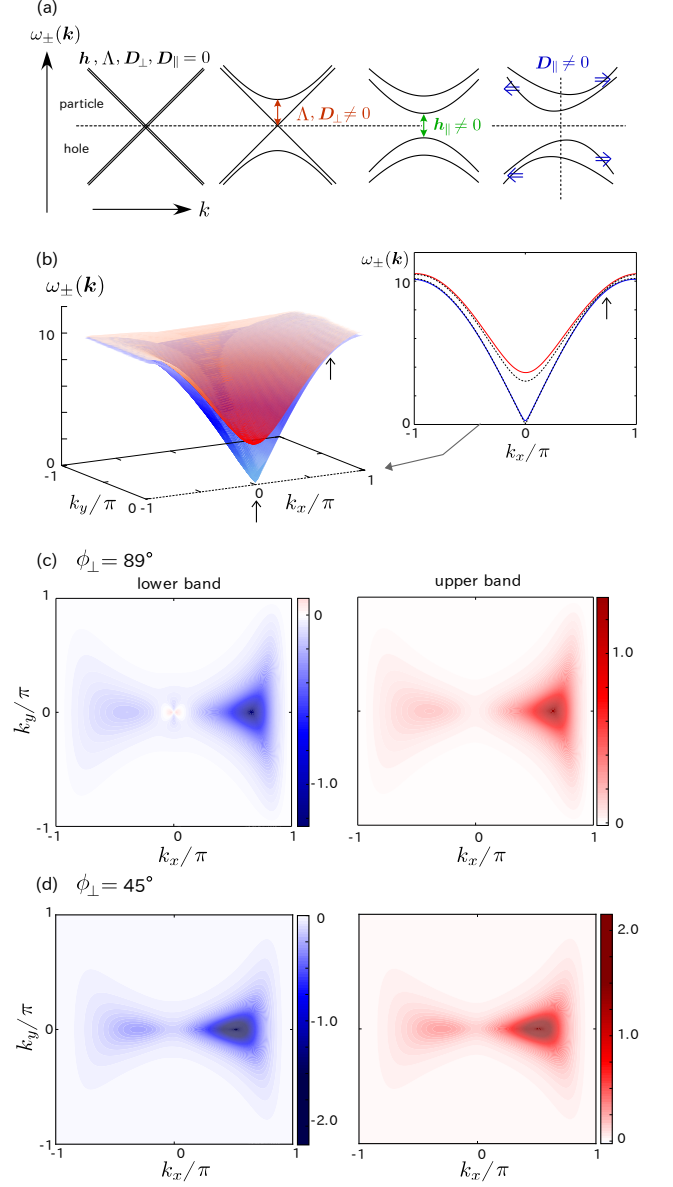


FIG. 4. (a) Schematic illustration of how the magnon bands are modified by the model parameters. (b) Magnon bands $\omega_{\pm}(\mathbf{k})$ of $k_y \leq 0$ at $D_{\parallel} = D_{\perp} = 0.2$, $\Lambda = 0.05$, $\phi_{\parallel} = 0$, $\phi_{\perp} = 89^\circ$. The right panel shows the cross sections of the magnon bands along the $k_y = 0$ line, where the broken and solid lines are $\mathbf{h}_{\perp} = \mathbf{0}$ and $\neq \mathbf{0}$ cases, respectively. When $\theta_{\perp} = 0$ ($\mathbf{h}_{\perp} = \mathbf{0}$), there is a band touching point along the k_x -axis. The finite θ_{\perp} opens a gap between upper and lower bands. (c)-(d) Density plot of the Berry curvature of the lower and upper bands, where we take (c) $\phi_{\perp} = 89^\circ$ and (d) 45° .

when the spins cant in the out-of-plane direction due to $\mathbf{h}_{\perp} \neq \mathbf{0}$, following the mechanism we discussed in §.II C.

We first show in Figs. 4(a) and 4(b) a schematic illustration of the magnon bands and the typical magnon dispersion of Eq.(1), respectively. In the Heisenberg antiferromagnet with $D_{\perp} = D_{\parallel} = 0$, $\Lambda = 0$, and $\mathbf{h} = \mathbf{0}$, a well-known doubly degenerate dispersion appears which

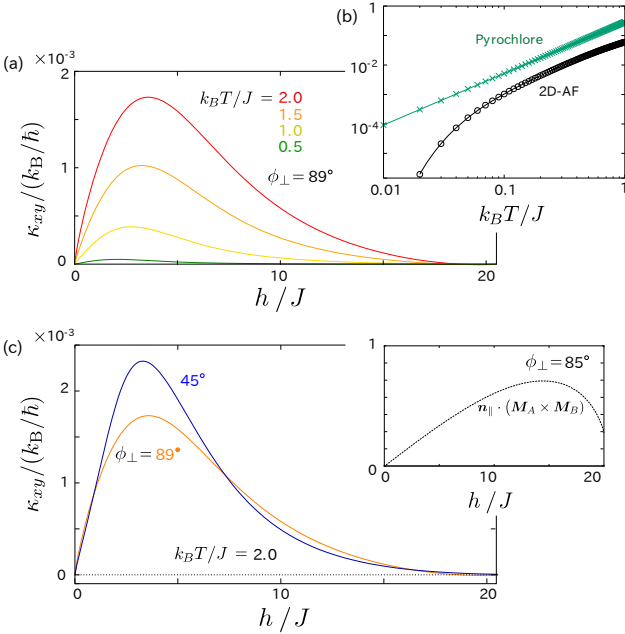


FIG. 5. In-plane thermal Hall conductivity $\kappa_{xy}/(k_B/\hbar)$. (a) Magnetic field $h = |\mathbf{h}|$ dependence at several temperatures when $\phi_{\perp} = 89^\circ$, (b) the temperature dependence at $\phi_{\perp} = 89^\circ$, and (c) the comparison for two different field angles $\phi_{\perp} = 45^\circ$ and 89° . (b) The comparison with the case of pyrochlore magnets in Ref.[7] that follows $\propto T^{7/2}$, which we calculated for $J = 1.0$, $S = 1/2$, $D = 0.32$, and $H = +0$ using their formula. The DM interactions defined in Fig. 2(a) have the Dresselhaus-type geometry. The Rashba types of DM interactions are obtained by converting the directions of the uniform DM vectors along the δ_2 -directions upside down, in which case κ_{xy} becomes negative with the same amplitude.

is linear in k around the Γ -point. When $\Lambda > 0$, the degeneracy is lifted and only the lower band remains zero at the Γ -point. By the introduction of \mathbf{D}_{\perp} (or either \mathbf{h}_{\parallel}), the spins are canted in-plane ($\theta_{\parallel} \neq 0$), and due to $\mathbf{D}_{\parallel} \neq 0$ the nonreciprocity appears⁷⁶. At $h_{\perp} = 0$, there is an accidental band touching point⁸³ along the k_x -axis ($k_y = 0$) indicated by arrows in Fig.4(b), besides the trivial degeneracy with the hole bands on the bottom (Γ -point). The former degeneracy is lifted by $\mathbf{h}_{\perp} \neq \mathbf{0}$, and the latter by $\mathbf{h}_{\parallel} \neq \mathbf{0}$.

We show in Fig. 4(c) the density plot of the Berry curvature for $\phi_{\parallel} = 0$ and $\phi_{\perp} = 89^\circ$ (the magnetic field almost perpendicular to the plane). One can see the enhancement of $\Omega_{xy}^{(\pm)}(\mathbf{k})$ at finite k_x off the Γ -point. This enhancement takes place in the vicinity of the \mathbf{k} -point where the band touching is observed at $\mathbf{h}_{\perp} = \mathbf{0}$. Then the two bands, which basically have different symmetry in the contributions from A- and B-sublattices, mix and generate a large $\Omega_{xy}^{(\pm)}(\mathbf{k})$. When the gap is small, the degree of the band mixing and the value of $\Omega_{xy}^{(\pm)}(\mathbf{k})$ are large, which are gradually suppressed by the increase of \mathbf{h}_{\perp} . In contrast, the particle-hole contact at the Γ -point

does not contribute much to $\Omega_{xy}^{(\pm)}(\mathbf{k})$ when $\mathbf{h}_{\perp} \neq \mathbf{0}$, since these two bands have the same symmetry in terms of A- and B-sublattice degrees of freedom.

We also show in Fig. 4(d) the Berry curvature at $\phi_{\perp} = 45^\circ$. The in-plane element, \mathbf{h}_{\parallel} , first works to shift the (nearly) band-touching point in the $-k_x$ -direction. Therefore at this field angle, the region where $\Omega_{xy}^{(\pm)}(\mathbf{k})$ takes the maximum shifts to lower energy levels, and its amplitude is enhanced (since $h_{\perp} = |\mathbf{h}_{\perp}| = h/\sqrt{2} < h$). A further increase of h_{\parallel} shifts the band-touching point from the center toward the other edge of the Brillouin zone, and suppresses $\Omega_{xy}^{(\pm)}(\mathbf{k})$. The details of how the Berry curvature develops when the magnetic field is varied is shown in Appendix D.

B. Thermal Hall effect

The thermal Hall conductivity Eq.(13) is calculated based on the above mentioned band structures. Figure 5 shows κ_{xy} as a function of magnetic field h for several different temperatures. The enhancement of κ_{xy} by $k_B T$ is due to the thermal excitation following the bosonic distribution function. The comparison with the thermal Hall conductivity obtained for the previously reported pyrochlore ferromagnet⁷ is shown in Fig. 5(b); the pyrochlore ferromagnet has only a small magnetic field dependence, and a clear $T^{7/2}$ -dependence is observed. Notice that the $k_B T$ is scaled by J , which depends much on the material parameters (also D as well), so that the direct comparison of the absolute values of κ_{xy} between the two systems does not make sense. The distinct feature of our antiferromagnet is the rapid growth of κ_{xy} , beyond the simple power of T at temperatures lower than $k_B T \lesssim 0.1J$, which is actually the target temperature range of measurements in laboratories. This should come from the nearly gapless excitation of the lower magnon branch, where the tail of the peak of $\Omega_{xy}^{(\pm)}(\mathbf{k})$ extending from the band touching point at higher energy has a non-negligible contribution. The gapped pyrochlore ferromagnet does not have such low energy modes. In fact, as the temperature increases, κ_{xy} of our antiferromagnets extrapolates to $T^{7/2}$ -behavior of the pyrochlore ferromagnets, where the contribution from the Berry curvature at the higher magnon bands dominates.

Figure 5(c) shows the h -dependence of κ_{xy} for another field angle 45° . At $h = 0$, we have exactly $\kappa_{xy} = 0$ since $\theta_{\perp} = 0$. When a finite h (with $\phi_{\perp} > 0$) is introduced, the spins start to cant and the solid angle shown in Fig.3(b) increases and so as $\Omega_{xy}^{(\pm)}(\mathbf{k})$, which explains the rapid growth of κ_{xy} . The functional form of the solid angle at small h given in the inset actually resembles that of κ_{xy} . As we discussed in Figs.5(c) and 5(d), rotating the angle from 89° to 45° shifts the point with maximum $\Omega_{xy}^{(\pm)}(\mathbf{k})$ to lower energy levels, which then works to enhance κ_{xy} . The further increase of field or field angle then pushes this maximum point to higher energies (see Appendix D)

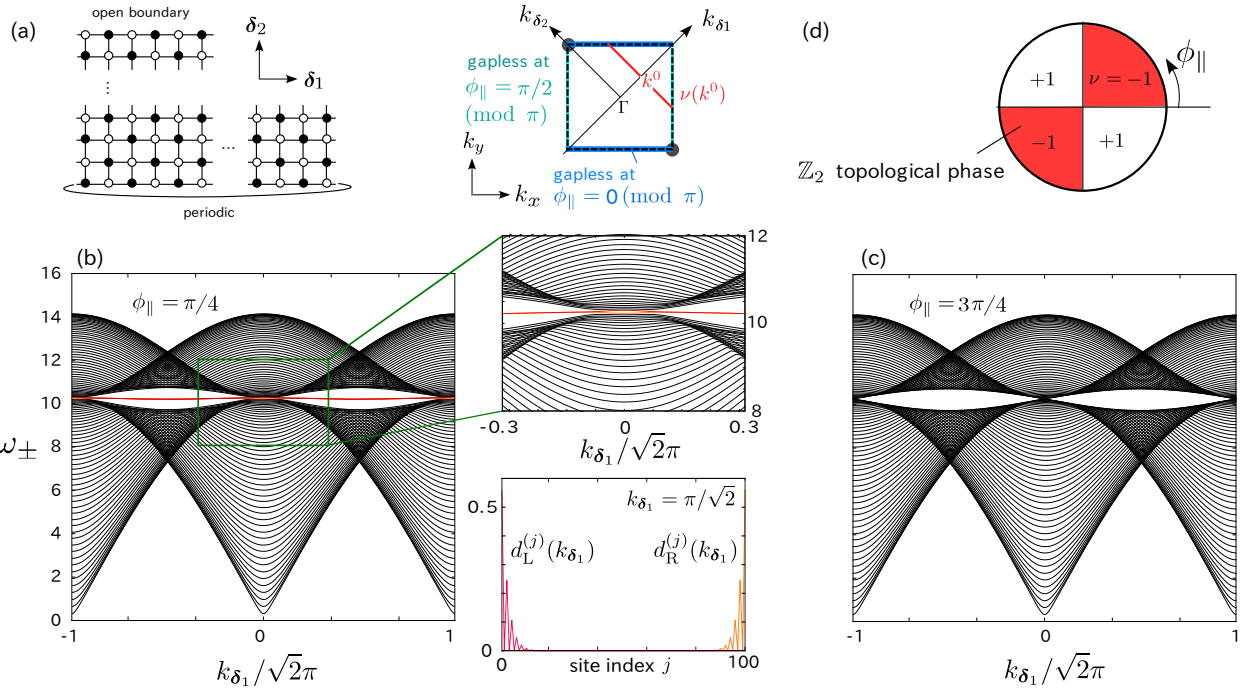


FIG. 6. (a) Lattice with periodic boundary in the δ_1 -direction and open boundary at $\delta_2 = 0$ and $2L$. The topological invariant is defined independently from the calculation of the edge modes along k_{δ_2} line for each fixed k_{δ_1} in the Brillouin one, avoiding the gapless point at $k_{\delta_1} = 0, \pm\sqrt{2}\pi$. (b), (c) The energy dispersion of magnons, $\omega_{\pm}(k_{\delta_1})$, consisting of $2L$ lines, calculated for the lattice in panel (a). The red/orange solid lines present only in (b) are the topologically protected edge modes. We take $L = 50$, $D_{\perp} = 0.2$, $D_{\parallel} = 0.2$, $\Lambda = 0.05$, $h = 14.0$, with $\phi_{\perp} = 89^\circ$ and (b) $\phi_{\parallel} = \pi/4$ and (c) $\phi_{\parallel} = 3\pi/4$. The levels near the modes are magnified in the middle panel, and in the lower middle panel, the local density of states of the two edge modes, $d_{L/R}^{(j)}(k_{\delta_1} = \pi/\sqrt{2})$ along the δ_2 -direction in real space are shown. (d) Phase diagram as a function of ϕ_{\parallel} classifying the $\nu = \pm 1$ regions, corresponding to the topological and trivial phases.

and κ_{xy} becomes gradually suppressed, even though the solid angle continues to increase up to $h/J \sim 15$.

C. Edge mode in the \mathbb{Z}_2 topological phase

We finally show the existence of topological phase characterized by the \mathbb{Z}_2 topological invariant. For simplicity, we set the field nearly perpendicular to the plane, $\phi_{\perp} = 89^\circ$. The in-plane direction of the classical spins in the ground state is determined by a small \mathbf{h}_{\parallel} . We show that ϕ_{\parallel} plays an important role. Note that the magnitude of \mathbf{h}_{\parallel} is not important as it simply serves to determine the in-plane angle of the magnetic moment.

The calculation on edge modes (see §.IID) are based on the lattice of width $2L$ with open edges. As shown in Fig.6(a), we take the periodic boundary in the δ_1 -direction and obtain $2L$ sets of particle and hole bands defined along the k_{δ_1} -direction in momentum space. Figures 6(b) and 6(c) display the particle bands, $\omega_{\pm}(k_{\delta_1}) \geq 0$ for $\phi_{\parallel} = \pi/4$ and $3\pi/4$, respectively. Although they look alike, only the former affords topologically protected edge modes (red and orange lines) inside the gap. The topologically protected edge modes disappear at

$k_{\delta_1} = 0, \pm\sqrt{2}\pi$, which corresponds to the corner of the Brillouin zone, where the band gap closes. The distributions of these edge states in real space described by the local density of states $d_{L/R}^{(j)}(k_{\delta_1})$, are shown in the inset of Fig.6(b)(bottom panel in the middle) along the δ_2 -direction. [For details of $d_{L/R}^{(j)}(k_{\delta_1})$ see Appendix A.] One can see that the left and right edge states are localized over ~ 5 lattice spacings from the open edges.

We now examine the topological invariant to confirm the above findings. When $\phi_{\parallel} = n\pi/2$ (with integer n), there is always a band degeneracy along either the $k_x = \pm\pi$ line ($n = \text{odd}$) or the $k_y = \pm\pi$ line ($n = \text{even}$) at the Brillouin zone boundary. Otherwise, the bands are gapped except at the corner of the Brillouin zone, and we can define a winding number as in Eq. (24). The winding number is obtained as,

$$W(k_{\delta_1}) = \pi M, \quad M \in \mathbb{Z} \quad (27)$$

and accordingly, the \mathbb{Z}_2 topological invariant becomes,

$$\nu(k_{\delta_1}) = \begin{cases} -1 & (\phi_{\parallel} = (0, \frac{\pi}{2}), (\pi, \frac{3\pi}{2})) \\ +1 & (\phi_{\parallel} = (\frac{\pi}{2}, \pi), (\frac{3\pi}{2}, 2\pi)) \end{cases} \quad (28)$$

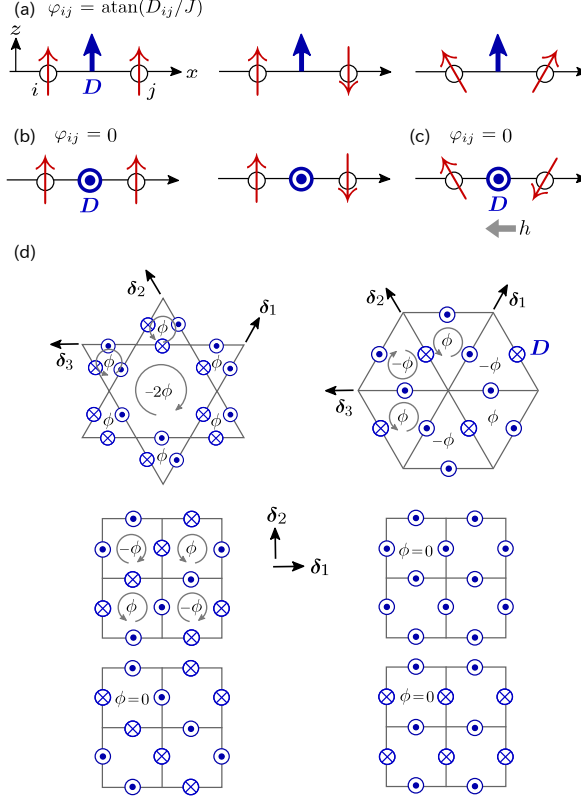


FIG. 7. (a)-(c) Schematic illustration of the coupling of DM interactions with collinear or nearly collinear magnetic structures. The representative cases where the magnetic moments are (a) parallel and (b) perpendicular to the DM interaction, where the former affords a local phase φ_{ij} , but the latter does not. (c) When the antiferromagnetic moments cant within the plane perpendicular to \mathbf{D} , we find a finite Berry curvature although $\varphi = 0$, which is explained in Fig.3. (d) The 2D lattices with DM interactions. The flux inside the closed loop \mathcal{C} is defined as, $\phi = \sum_{\mathcal{C}} \varphi_{ij}$. The net flux is zero in all cases. The thermal Hall effect is present only in the kagome lattice, since it contains two inequivalent loops in the unit cell.

The phase diagram regarding ϕ_{\parallel} is shown in Fig.6(d); there is a topological phase transition at $\phi_{\parallel} = n\pi/2$ (with integer n), where the band degeneracy actually takes place, and the diagram is separated into the topological and trivial regions. Thus, regarding Figs.6(b) and 6(c), only the former has the topologically protected edge modes.

IV. DISCUSSION

We demonstrated that the thermal Hall conductivity and topologically protected edge modes appear due to the nonvanishing Berry curvature in a square lattice antiferromagnet, when the magnetic moments cant and point in the direction perpendicular to the DM vector as shown in

Fig.1(b). We stressed in §.I that the conventional mechanism using a U(1) gauge field in Fig.1(a) does not apply to square lattice models. To further clarify this point, we classify the role of DM interactions by the way they align and by the lattice geometries based on the established idea given in Refs.[7] and [8].

Let us discuss the simplest part of the Hamiltonian including only the Heisenberg exchange and the DM interaction,

$$\begin{aligned} \mathcal{H}_{ij} &= JS_i \cdot S_j + D_{ij}^z e_z \cdot [S_i \times S_j] \\ &= J_{\text{eff}} (e^{-i\varphi_{ij}} S_i^+ S_j^- + e^{i\varphi_{ij}} S_i^- S_j^+) + JS_i^z S_j^z, \end{aligned} \quad (29)$$

with $\varphi_{ij} = \text{atan}(D_{ij}^z/J)$ and $J_{\text{eff}} = \sqrt{J^2 + (D_{ij}^z)^2}/2$. The transfer integral of magnons, $J_{\text{eff}} e^{i\varphi_{ij}}$, has a finite phase factor when $D_{ij}^z \neq 0$.

Figures 7(a)-7(c) show the relative relationships between the ordered magnetic moments and the DM vectors. When the DM vector has a finite element parallel to the ordered magnetic moments, the kinetics of magnons couples to \mathbf{D} and gains a phase φ_{ij} . Here, we stress that when \mathbf{D} is perpendicular to the moments [Figs.7(b) and 7(c)], this mechanism does not hold as we showed explicitly in Figs.3(d) and 3(e).

Now, we consider 2D lattices shown in Fig.7(d). Since the sign of D_{ij} changes by converting i and j , we define the direction $i \rightarrow j$ as δ_{γ} , $\gamma = 1, 2, 3$, in the figure to fix the direction in the figure. Here, we prepare several types of lattices with the staggered and uniform DM interactions [see Figs. 2(b) and 2(c)]: a kagome and a triangular lattice for the former and the latter, respectively, and a square lattice for both. Let us take a closed loop, \mathcal{C} , along the bonds in each of these lattices. When $\varphi_{ij} \neq 0$, a fictitious magnetic flux, $\phi = \sum_{\mathcal{C}} \varphi_{ij}$, is generated, where we take the counterclockwise direction in the summation. The net flux is zero in all cases but the thermal Hall conductivity is finite in the kagome lattice and zero in the square and triangular lattices.

The reason is explained as follows. In the square and triangular lattices, there are geometrically equivalent loops in the unit cell, and there exists a symmetry operation that does not change the flux pattern but converts the sign of the thermal Hall conductivity. This straightforwardly implies that the thermal Hall conductivity is zero. Note that this symmetry operation does not change the effective Hamiltonian of free bosons in the presence of fluxes.

This argument is illustrated more precisely as follows. Let us consider a general $2n \times 2n$ BdG Hamiltonian, $H_{\text{BdG}}(\mathbf{k})$, of magnons where n denotes the number of degrees of freedom in a unit cell. Suppose that there is an operator represented by the $2n \times 2n$ unitary matrix, \mathcal{O} , describing the above mentioned symmetry operation in the system, which satisfies,

$$\mathcal{O} K H_{\text{BdG}}(\mathbf{k}) K^{-1} \mathcal{O}^{\dagger} = H_{\text{BdG}}(\mathbf{k}), \quad (30)$$

together with $[\mathcal{O}, \tilde{\Sigma}^z] = 0$ and $\tilde{\Sigma}^z = \tau^z \otimes 1_{n \times n}$. For example, $\mathcal{O} K$ can be the exchange of the sublattices and

the conversion of the flux associated with that operation. If Eq.(30) is fulfilled and if the energy bands are not degenerate at \mathbf{k} , one can take the eigenvector, $\mathbf{t}_\mu(\mathbf{k})$ ($\mu = 1, 2, \dots, 2n$), of $H_{\text{BdG}}(\mathbf{k})$ in the following form,

$$\mathbf{t}_\mu(\mathbf{k}) = e^{i\varphi_\mu(\mathbf{k})} \mathcal{O} \mathbf{t}_\mu^*(\mathbf{k}), \quad (31)$$

where $\varphi_\mu(\mathbf{k}) \in \mathbb{R}$ is some proper choice of a phase factor. From Eq.(31) and from the normalization condition, $\mathbf{t}_\mu^\dagger(\mathbf{k}) \tilde{\Sigma}^z \mathbf{t}_\mu(\mathbf{k}) = (\tilde{\Sigma}^z)_{\mu,\mu}$, it is straightforward to see that the Berry curvature of the μ -th band satisfies

$$\begin{aligned} \Omega_{xy}^{(\mu)}(\mathbf{k}) &= -2(\Sigma^z)_{\mu,\mu} \text{Im} \left[\frac{\partial \mathbf{t}_\mu^\dagger(\mathbf{k})}{\partial k_x} \tilde{\Sigma}^z \frac{\partial \mathbf{t}_\mu(\mathbf{k})}{\partial k_y} \right] \\ &= -2(\Sigma^z)_{\mu,\mu} \text{Im} \left[\frac{\partial \mathbf{t}_\mu^T(\mathbf{k})}{\partial k_x} \mathcal{O}^\dagger \tilde{\Sigma}^z \mathcal{O} \frac{\partial \mathbf{t}_\mu^*(\mathbf{k})}{\partial k_y} + (\text{real}) \right] \\ &= -\Omega_{xy}^{(\mu)}(\mathbf{k}). \end{aligned} \quad (32)$$

In this way, we find $\Omega_{xy}^{(\mu)}(\mathbf{k}) = 0$ when there exists an operator \mathcal{O} that satisfies Eq.(30). The actual example is discussed previously in Ref.[7]. From Eqs.(14) and (15), our antiferromagnet *without* \mathbf{D}_\parallel satisfies Eq.(30) with $\mathcal{O} = (\tau^0 \otimes \sigma^x)$, that makes $\Omega_{xy}^{(\mu)}(\mathbf{k}) = 0$.

Now, we go back to the lattices shown in Fig.7(d). In the square and triangular lattices with finite fluxes, a π rotation around the δ_1 axis connects different loops of the same size and shape and serves as \mathcal{O} . For the three cases of a square lattice in the lower part of the figure, the Berry curvature is already zero, whereas in the kagome lattice, there is no such symmetry operation \mathcal{O} that connects inequivalent loops in the unit cell, and the Berry curvature remains finite^{7,8}.

The above discussion was previously applied to centrosymmetric ferromagnets with SIS. The SIS broken systems with uniform DM interaction were thus overlooked. This shall be because, if the SIS is broken and the DM interaction aligns uniformly [Fig.3(c)] the flux itself is absent as we see in the lower right panels of Fig.7(d).

V. SUMMARY

We showed theoretically that the 2D inversion-symmetry broken square lattice antiferromagnet hosts the thermal Hall effect and the topologically protected edge modes. These two properties are based on the finite Berry curvature of magnon bands. The conventionally established way to generate a finite Berry curvature was to generate a U(1) gauge field or a fictitious flux discussed

in the previous section. The \mathbf{D} -vector *parallel* to the moments couples to the magnons as a vector potential and generates a local phase in their hoppings. By the proper choice of the geometry of lattices, which are the corner shared kagome and pyrochlore, one could avoid the cancellation of the effect of the U(1) gauge field. However, within that framework, our square lattice geometry can never afford a nonvanishing Berry curvature, since there exists a symmetry operation that cancels out the effect of U(1) gauge field together with the TRS.

In our antiferromagnet, a different mechanism works; there are two species of magnons for two sublattices, and they serve as a pseudo-spin degrees of freedom. When a magnon hops from the A-sublattice to the neighboring B-sublattice, it accompanies a pseudo-spin flip, represented by the Pauli matrix, $i\sigma_y$. When the SIS is broken, the hoppings of magnons to the left and right neighbors become antisymmetric and couple to the DM vector via opposite sign as $-i\sigma_y$ and $+i\sigma_y$, respectively. It resembles the antisymmetric hopping of the Rashba electrons accompanying a spin flip in the SU(2) gauge field, where an anomalous Hall effect occurs from the emergent Berry curvature of electron bands. Therefore, our uniform DM vector can be regarded as a pseudo-spin orbit coupling of magnons. This picture is rather simplified but makes it straightforward to understand why our system generates a nonvanishing Berry curvature. We showed in more detail that to activate the couplings with the DM vector, one needs to control the antiferromagnetic moments to point in the direction *perpendicular* to the \mathbf{D} -vectors, and to make it noncollinear by the magnetic field.

The touching point (with a tiny gap) of two magnon bands appears at the middle of the energy bands, which is the point where the Berry curvature is enhanced. Since the antiferromagnetic magnon bands have low energy branches near the zero energy level, the tail of the Berry curvature extending from this high energy point allows for the rapid increase of the thermal Hall conductivity beyond the powers of T , in sharp contrast to the $T^{7/2}$ -dependence in the pyrochlore ferromagnets. We also demonstrated that the topological phase is feasible in this system⁸⁴, and found that the topological phase transition characterized by the winding number is controlled by the rotation of the in-plane field angle.

ACKNOWLEDGMENTS

We acknowledge discussions with Y. Onose and Y. Iguchi and Y. Nii and K. Penc. This work is supported by JSPS KAKENHI Grants Numbers No. JP17K05533, No. JP17K05497, No. JP17H02916, and No. JP18H01173.

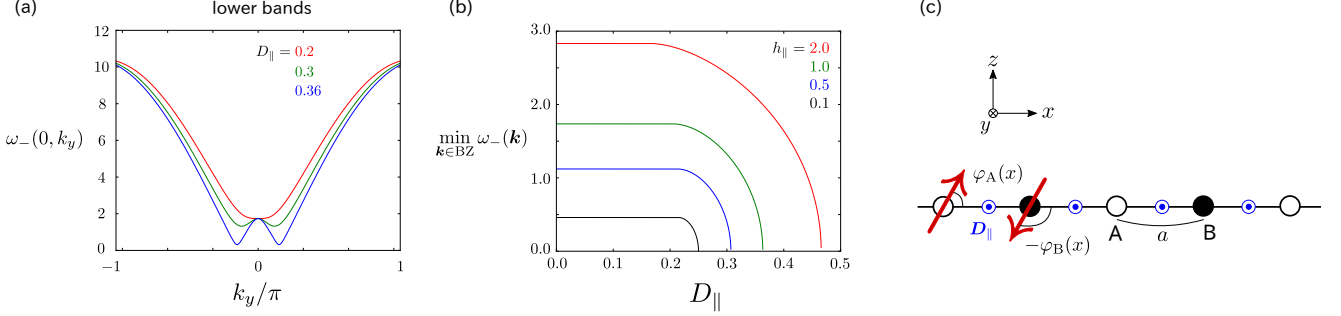


FIG. 8. (a) Lower magnon bands of Eq.(1) for several different values of D_\parallel , where we take $J = 1.0$, $D_\perp = 0.2$, $\Lambda = 0.05$, $h = 1.0$, and $\phi_\parallel = \phi_\perp = 0$. The instability of the canted two sublattice antiferromagnet to the incommensurate state occurs when the bottom of the bands fulfill $\omega_-(\mathbf{k} \neq 0) = 0$, at $D_\parallel \simeq 0.363$. (b) The minimum energy of the magnon bands as a function of uniform DM interaction D_\parallel . The instability takes place when these lines fall down to zero. For all \mathbf{h} with $D_\perp = D_\parallel = 0.2$ and $\Lambda = 0.05$, the two sublattice antiferromagnetic order is the stable ground state. (c) 1D antiferromagnetic chain with the uniform DM interaction and the easy-plane magnetic anisotropy.

Appendix A: Spin texture in the ground state

Our theory is built on the classical ground state with two-sublattice antiferromagnetic ordering. To verify the stability of this ground state, we estimate the critical value of D_\parallel , at which there exists a transition from our canted antiferromagnetic order to an incommensurate magnetic order. We first numerically examine Eq.(1) and obtain the critical value of D_\parallel . Figure 8(a) shows the variation of lower magnon bands for different choices of D_\parallel , where the other parameters are fixed to the ones we used in the main text, $J = 1.0$, $D_\perp = 0.2$, $\Lambda = 0.05$, and $h_\parallel = 1.0$. With increasing D_\parallel the bottom of the band at nonzero \mathbf{k} goes down and reaches the zero energy level at the critical value, $D_\parallel \sim 0.363$. In Fig.8(b) the minimum of ω_- is plotted as a function of D_\parallel for several choices of h_\parallel . The critical values of D_\parallel are the points where these lines fall down to the zero energy level. These results indicate that the system takes the stable antiferromagnetic ground state for a wide range of parameters including the ones we chose. We also see that both D_\perp and h_\parallel stabilizes the canted antiferromagnetic ground state against D_\parallel .

One can further analytically obtain the instability point for simpler cases. Let us consider a 1D antiferromagnet with a uniform DM interaction and an easy-plane magnetic anisotropy, whose Hamiltonian is given as,

$$\mathcal{H} = J \sum_{j=1}^N \mathbf{S}_j \cdot \mathbf{S}_{j+1} + \sum_{j=1}^N \mathbf{D}_\parallel \cdot [\mathbf{S}_j \times \mathbf{S}_{j+1}] + \Lambda \sum_{j=1}^N (S_j^z)^2, \quad (\text{A1})$$

where $\mathbf{D}_\parallel = -D_\parallel \mathbf{e}_y$, and we take the periodic boundary condition. The following discussion can be applied to our 2D antiferromagnet, if we regard the δ_1 - or δ_2 -direction as x -direction in Fig.8(c).

In the following, we neglect the staggered DM interaction, D_\perp , and the magnetic field, \mathbf{h} , for simplicity. Without the loss of generality, one can assume that the direction of the ordered moments varies slowly in space, and describe the classical moments as $\mathbf{S}_i = S \mathbf{n}_A(x_i)$ for the A-sublattice and $\mathbf{S}_j = S \mathbf{n}_B(x_j)$ for the B-sublattice, where $\mathbf{n}_{A/B}(x)$ is the continuous field and satisfies $(\mathbf{n}_{A/B}(x))^2 = 1$. Then the Hamiltonian is written as,

$$\mathcal{H} \simeq JS^2 a \int_0^L dx \left[\frac{1}{a^2} \mathbf{n}_A \cdot \mathbf{n}_B - \frac{1}{2} \partial_x \mathbf{n}_A \cdot \partial_x \mathbf{n}_B - \frac{D_\parallel}{Ja} [\mathbf{n}_A \times \partial_x \mathbf{n}_B]^y + \frac{\Lambda}{2Ja^2} \{(n_A^z)^2 + (n_B^z)^2\} \right], \quad (\text{A2})$$

where $L = Na$ and a is a lattice constant (see Fig.8(c)). For the collinear antiferromagnetic order within the easy-plane (xy -plane) with uniformly distributed $\mathbf{n}_A = -\mathbf{n}_B$, the energy is given by

$$E_{\text{col}} = -JNS^2. \quad (\text{A3})$$

Now we consider the case where the spins are pointing in the xz -plane. The following calculation is similar to the one for the chiral soliton lattice⁸⁶. The continuous field, $\mathbf{n}_{A/B}(x)$, can be written as

$$\mathbf{n}_A(x) = (\cos \varphi_A(x), 0, \sin \varphi_A(x)), \quad (\text{A4})$$

$$\mathbf{n}_B(x) = (\cos \varphi_B(x), 0, \sin \varphi_B(x)), \quad (\text{A5})$$

and the Hamiltonian can be written using $\varphi_{\pm}(x) = \varphi_A(x) \pm \varphi_B(x)$ as

$$\mathcal{H} \simeq E_{\text{col}} + JS^2a \int_0^L dx \left[\left\{ -\frac{1}{8}(\partial_x \varphi_+)^2 + \frac{1}{8}(\partial_x \varphi_-)^2 + \frac{D_{\parallel}}{2Ja}(\partial_x \varphi_+ - \partial_x \varphi_-) \right\} \cos \varphi_- + \frac{\Lambda}{2Ja^2}(1 - \cos \varphi_+ \cos \varphi_-) \right]. \quad (\text{A6})$$

For the field $\varphi_{\pm}(x)$ representing a stationary point, $\delta \mathcal{H} / \delta \varphi_{\pm}(x) = 0$ is satisfied. This gives,

$$\left(\frac{1}{4} \partial_x^2 \varphi_+ + \frac{\Lambda}{2Ja^2} \sin \varphi_+ \right) \cos \varphi_- - \left(\frac{1}{4} \partial_x \varphi_+ - \frac{D_{\parallel}}{2Ja} \right) (\partial_x \varphi_-) \sin \varphi_- = 0, \quad (\text{A7})$$

$$\left(\frac{1}{8}(\partial_x \varphi_+)^2 + \frac{1}{8}(\partial_x \varphi_-)^2 - \frac{D_{\parallel}}{2Ja}(\partial_x \varphi_+) + \frac{\Lambda}{2Ja^2} \cos \varphi_+ \right) \sin \varphi_- - \frac{1}{4}(\partial_x^2 \varphi_-) \cos \varphi_- = 0. \quad (\text{A8})$$

Assuming that $\mathbf{n}_A(x)$ and $\mathbf{n}_B(x)$ are locally antiparallel for all given x , i.e. $\varphi_-(x) = \pi$, the above condition can be written as,

$$\frac{d^2}{dx^2} \varphi_+(x) = -\frac{2\Lambda}{Ja^2} \sin \varphi_+(x), \quad (\text{A9})$$

and one finds,

$$\varphi_+(x) = 2\text{am} \left(\sqrt{\frac{2\Lambda}{Ja^2}} \frac{x}{m}, m \right), \quad (\text{A10})$$

where $\text{am}(x, m)$ is the Jacobi amplitude function, and the value m satisfies $0 \leq m \leq 1$. For a sufficiently long chain length L , that satisfies $(\varphi_A(L) - \varphi_A(0))/2\pi \in \mathbb{N}$, the energy is given by

$$E_{\text{chiral}}(m) = E_{\text{col}} + \Lambda N S^2 \left(1 - \frac{1}{m^2} \right) + \frac{2\Lambda N S^2}{m K(m)} \left(\frac{E(m)}{m} - \frac{\pi}{2} \frac{D_{\parallel}}{J} \sqrt{\frac{J}{2\Lambda}} \right), \quad (\text{A11})$$

where $K(m)$ and $E(m)$ are the complete elliptic integral of the first kind and second kind, respectively. The derivative of $E_{\text{chiral}}(m)$ with respect to m is calculated as,

$$\frac{dE_{\text{chiral}}(m)}{dm} = -\frac{2\Lambda N S^2}{m^2(1-m^2)} \frac{E(m)}{K^2(m)} \left[\frac{E(m)}{m} - \frac{\pi}{2} \frac{D_{\parallel}}{J} \sqrt{\frac{J}{2\Lambda}} \right]. \quad (\text{A12})$$

The solution of $dE_{\text{chiral}}(m)/dm|_{m=m^*} = 0$ satisfies the following condition,

$$\frac{E(m^*)}{m^*} = \frac{\pi}{2} \frac{D_{\parallel}}{J} \sqrt{\frac{J}{2\Lambda}}, \quad (\text{A13})$$

and the ground state energy is given by

$$E_{\text{chiral}}(m^*) = E_{\text{col}} + \Lambda N S^2 \left(1 - \frac{1}{(m^*)^2} \right) \leq E_{\text{col}}. \quad (\text{A14})$$

Thus, if there exists a solution of Eq.(A13), the ground state is no longer in a collinear antiferromagnetic state. The condition to exclude such solution is to have D_{\parallel} as small as,

$$\frac{D_{\parallel}}{J} \leq \frac{2}{\pi} \sqrt{\frac{2\Lambda}{J}}, \quad (\text{A15})$$

since $E(m)/m \geq 1$. When $J = 1.0$ and $\Lambda = 0.05$, Eq.(A15) can be rewritten as $D_{\parallel} \leq 2/\sqrt{10\pi} \simeq 0.2013$. If we introduce $D_{\perp} \neq 0$ and $h_{\parallel} \neq 0$, the critical value of D_{\parallel} will increase. Therefore, it gives the lower bound of the phase boundary. The value $D_{\parallel} = 0.2$ we adopted still remains below this lower bound.

Appendix B: Details of the spin wave analysis

We show the details of the results of the spin wave analysis in §.II B in the main text. The 2×2 matrices $\Xi_{\mathbf{k}}$ and $\Delta_{\mathbf{k}}$ in Eq.(8) are given by,

$$\Xi_{\mathbf{k}} = \xi^{(0)} \sigma^0 + \xi_{\mathbf{k}}^{(x)} \sigma^x + \xi_{\mathbf{k}}^{(y)} \sigma^y, \quad (\text{B1})$$

$$\Delta_{\mathbf{k}} = \Delta^{(0)} \sigma^0 + \Delta_{\mathbf{k}}^{(x)} \sigma^x + \Delta_{\mathbf{k}}^{(y)} \sigma^y, \quad (\text{B2})$$

where

$$\begin{aligned} \xi^{(0)} &= 4JS(\cos 2\theta_{\parallel} \cos^2 \theta_{\perp} - \sin^2 \theta_{\perp}) + 4D_{\perp} S \sin 2\theta_{\parallel} \cos^2 \theta_{\perp} + \Lambda S(1 - 3\sin^2 \theta_{\perp}) \\ &\quad + h(\sin \phi_{\perp} \sin \theta_{\perp} + \cos \phi_{\perp} \sin \theta_{\parallel} \cos \theta_{\perp}), \end{aligned} \quad (\text{B3})$$

$$\xi_{\mathbf{k}}^{(x)} = -4JS\gamma_{\mathbf{k}}(\sin^2 \theta_{\parallel} - \cos^2 \theta_{\parallel} \sin^2 \theta_{\perp}) + 4D_{\perp} S \gamma_{\mathbf{k}} \sin \theta_{\parallel} \cos \theta_{\parallel} (1 + \sin^2 \theta_{\perp}) - 2D_{\parallel} S g_{1,\mathbf{k}} \sin \theta_{\parallel} \cos \theta_{\perp}, \quad (\text{B4})$$

$$\xi_{\mathbf{k}}^{(y)} = -4JS\gamma_{\mathbf{k}} \sin 2\theta_{\parallel} \sin \theta_{\perp} + 4D_{\perp} S \gamma_{\mathbf{k}} \cos 2\theta_{\parallel} \sin \theta_{\perp} - D_{\parallel} S g_{1,\mathbf{k}} \cos \theta_{\parallel} \sin 2\theta_{\perp}, \quad (\text{B5})$$

$$\Delta^{(0)} = -\Lambda S \cos^2 \theta_{\perp}, \quad (\text{B6})$$

$$\Delta_{\mathbf{k}}^{(x)} = 4JS\gamma_{\mathbf{k}} \cos^2 \theta_{\parallel} \cos^2 \theta_{\perp} + 2D_{\perp} S \gamma_{\mathbf{k}} \sin 2\theta_{\parallel} \cos^2 \theta_{\perp}, \quad (\text{B7})$$

$$\Delta_{\mathbf{k}}^{(y)} = D_{\parallel} S g_{1,\mathbf{k}} \cos \theta_{\parallel} \sin 2\theta_{\perp} - 2iD_{\parallel} S g_{2,\mathbf{k}} \cos \theta_{\parallel} \cos \theta_{\perp}, \quad (\text{B8})$$

$$\gamma_{\mathbf{k}} = \frac{\cos \mathbf{k} \cdot \boldsymbol{\delta}_1 + \cos \mathbf{k} \cdot \boldsymbol{\delta}_2}{2}, \quad (\text{B9})$$

$$g_{1,\mathbf{k}} = \cos \phi_{\parallel} \frac{\sin \mathbf{k} \cdot \boldsymbol{\delta}_1 - \sin \mathbf{k} \cdot \boldsymbol{\delta}_2}{\sqrt{2}} - \sin \phi_{\parallel} \frac{\sin \mathbf{k} \cdot \boldsymbol{\delta}_1 + \sin \mathbf{k} \cdot \boldsymbol{\delta}_2}{\sqrt{2}} \quad (\text{B10})$$

$$g_{2,\mathbf{k}} = \cos \phi_{\parallel} \frac{\sin \mathbf{k} \cdot \boldsymbol{\delta}_1 + \sin \mathbf{k} \cdot \boldsymbol{\delta}_2}{\sqrt{2}} + \sin \phi_{\parallel} \frac{\sin \mathbf{k} \cdot \boldsymbol{\delta}_1 - \sin \mathbf{k} \cdot \boldsymbol{\delta}_2}{\sqrt{2}}. \quad (\text{B11})$$

The final analytical form of the magnon band is given as,

$$\omega_{\pm}(\mathbf{k}) = \frac{1}{2} \left(\sqrt{w_{\mathbf{k}}} \pm \sqrt{2P_{\mathbf{k}} + \frac{2Q_{\mathbf{k}}}{\sqrt{w_{\mathbf{k}}}} - w_{\mathbf{k}}} \right) \quad (\text{B12})$$

where $w_{\mathbf{k}}$, $P_{\mathbf{k}}$, $Q_{\mathbf{k}}$ are given explicitly as,

$$w_{\mathbf{k}} = \eta_{\mathbf{k}} + \zeta_{\mathbf{k}} + \frac{2}{3} P_{\mathbf{k}} \in \mathbb{R}, \quad (\text{B13})$$

$$\eta_{\mathbf{k}}^3 = \frac{1}{2} \left(L_{\mathbf{k}} + \sqrt{L_{\mathbf{k}}^2 - 4 \left(\frac{P_{\mathbf{k}}^2}{9} + \frac{4}{3} R_{\mathbf{k}} \right)^3} \right), \quad (\text{B14})$$

$$\zeta_{\mathbf{k}}^3 = \frac{1}{2} \left(L_{\mathbf{k}} - \sqrt{L_{\mathbf{k}}^2 - 4 \left(\frac{P_{\mathbf{k}}^2}{9} + \frac{4}{3} R_{\mathbf{k}} \right)^3} \right), \quad (\text{B15})$$

$$L_{\mathbf{k}} = -\frac{2}{27} P_{\mathbf{k}}^3 + \frac{8}{3} P_{\mathbf{k}} R_{\mathbf{k}} + Q_{\mathbf{k}}^2, \quad (\text{B16})$$

$$P_{\mathbf{k}} = 2(\xi^{(0)})^2 + (\xi_{\mathbf{k}}^{(x)})^2 + (\xi_{\mathbf{k}}^{(y)})^2 + (\xi_{-\mathbf{k}}^{(x)})^2 + (\xi_{-\mathbf{k}}^{(y)})^2 - 2(\Delta^{(0)})^2 - 2(\Delta_{\mathbf{k}}^{(x)})^2 - 2|\Delta_{\mathbf{k}}^{(y)}|^2, \quad (\text{B17})$$

$$Q_{\mathbf{k}} = 2\xi^{(0)} \{ (\xi_{\mathbf{k}}^{(x)})^2 + (\xi_{\mathbf{k}}^{(y)})^2 - (\xi_{-\mathbf{k}}^{(x)})^2 - (\xi_{-\mathbf{k}}^{(y)})^2 \} - 4\Delta^{(0)} \{ (\xi_{\mathbf{k}}^{(x)} - \xi_{-\mathbf{k}}^{(x)}) \Delta_{\mathbf{k}}^{(x)} - (\xi_{\mathbf{k}}^{(y)} + \xi_{-\mathbf{k}}^{(y)}) \text{Re} \Delta_{\mathbf{k}}^{(y)} \}, \quad (\text{B18})$$

$$\begin{aligned} R_{\mathbf{k}} = & \{ (\xi^{(0)})^2 - (\Delta^{(0)})^2 \}^2 - (\xi^{(0)})^2 \{ (\xi_{\mathbf{k}}^{(x)})^2 + (\xi_{\mathbf{k}}^{(y)})^2 + (\xi_{-\mathbf{k}}^{(x)})^2 + (\xi_{-\mathbf{k}}^{(y)})^2 + 2(\Delta_{\mathbf{k}}^{(x)})^2 + 2|\Delta_{\mathbf{k}}^{(y)}|^2 \} \\ & - 2(\Delta^{(0)})^2 \{ \xi_{\mathbf{k}}^{(x)} \xi_{-\mathbf{k}}^{(x)} - \xi_{\mathbf{k}}^{(y)} \xi_{-\mathbf{k}}^{(y)} + (\Delta_{\mathbf{k}}^{(x)})^2 + (\text{Re} \Delta_{\mathbf{k}}^{(y)})^2 - (\text{Im} \Delta_{\mathbf{k}}^{(y)})^2 \} \\ & + 4\xi^{(0)} \Delta^{(0)} \{ (\xi_{\mathbf{k}}^{(x)} + \xi_{-\mathbf{k}}^{(x)}) \Delta_{\mathbf{k}}^{(x)} - (\xi_{\mathbf{k}}^{(y)} - \xi_{-\mathbf{k}}^{(y)}) \text{Re} \Delta_{\mathbf{k}}^{(y)} \} \\ & + \{ \xi_{\mathbf{k}}^{(x)} \xi_{-\mathbf{k}}^{(x)} + \xi_{\mathbf{k}}^{(y)} \xi_{-\mathbf{k}}^{(y)} - (\Delta_{\mathbf{k}}^{(x)})^2 + |\Delta_{\mathbf{k}}^{(y)}|^2 \}^2 + (\xi_{-\mathbf{k}}^{(x)} \xi_{\mathbf{k}}^{(y)} - \xi_{\mathbf{k}}^{(x)} \xi_{-\mathbf{k}}^{(y)} + 2\Delta_{\mathbf{k}}^{(x)} \text{Re} \Delta_{\mathbf{k}}^{(y)})^2. \end{aligned} \quad (\text{B19})$$

The unnormalized eigenvector $(U_{\pm,A}(\mathbf{k}), U_{\pm,B}(\mathbf{k}), V_{\pm,A}(\mathbf{k}), V_{\pm,B}(\mathbf{k}))$ is

$$U_{\pm,A}(\mathbf{k}) = \left\{ (\xi_{-\mathbf{k}}^{(x)} + i\xi_{-\mathbf{k}}^{(y)})(\Delta_{\mathbf{k}}^{(x)} - i(\Delta_{\mathbf{k}}^{(y)})^*) - (\xi^{(0)} + \omega_{\pm}(\mathbf{k}))\Delta^{(0)} \right\} \frac{V_{\pm,A}(\mathbf{k})}{(\Delta^{(0)})^2 - (\Delta_{\mathbf{k}}^{(x)})^2 + \{(\Delta_{\mathbf{k}}^{(y)})^*\}^2} \\ + \left\{ (\xi^{(0)} + \omega_{\pm}(\mathbf{k}))(\Delta_{\mathbf{k}}^{(x)} - i(\Delta_{\mathbf{k}}^{(y)})^*) - (\xi_{-\mathbf{k}}^{(x)} - i\xi_{-\mathbf{k}}^{(y)})\Delta^{(0)} \right\} \frac{V_{\pm,B}(\mathbf{k})}{(\Delta^{(0)})^2 - (\Delta_{\mathbf{k}}^{(x)})^2 + \{(\Delta_{\mathbf{k}}^{(y)})^*\}^2}, \quad (\text{B20})$$

$$U_{\pm,B}(\mathbf{k}) = \left\{ (\xi^{(0)} + \omega_{\pm}(\mathbf{k}))(\Delta_{\mathbf{k}}^{(x)} + i(\Delta_{\mathbf{k}}^{(y)})^*) - (\xi_{-\mathbf{k}}^{(x)} + i\xi_{-\mathbf{k}}^{(y)})\Delta^{(0)} \right\} \frac{V_{\pm,A}(\mathbf{k})}{(\Delta^{(0)})^2 - (\Delta_{\mathbf{k}}^{(x)})^2 + \{(\Delta_{\mathbf{k}}^{(y)})^*\}^2} \\ + \left\{ (\xi_{-\mathbf{k}}^{(x)} - i\xi_{-\mathbf{k}}^{(y)})(\Delta_{\mathbf{k}}^{(x)} + i(\Delta_{\mathbf{k}}^{(y)})^*) - (\xi^{(0)} + \omega_{\pm}(\mathbf{k}))\Delta^{(0)} \right\} \frac{V_{\pm,B}(\mathbf{k})}{(\Delta^{(0)})^2 - (\Delta_{\mathbf{k}}^{(x)})^2 + \{(\Delta_{\mathbf{k}}^{(y)})^*\}^2}, \quad (\text{B21})$$

$$\frac{V_{\pm,A}(\mathbf{k})}{(\Delta^{(0)})^2 - (\Delta_{\mathbf{k}}^{(x)})^2 + \{(\Delta_{\mathbf{k}}^{(y)})^*\}^2} = \{(\xi^{(0)})^2 - (\omega_{\pm}(\mathbf{k}))^2\}(\Delta_{\mathbf{k}}^{(x)} - i(\Delta_{\mathbf{k}}^{(y)})^*) - \Delta^{(0)}(\xi_{\mathbf{k}}^{(x)} - \xi_{-\mathbf{k}}^{(x)} + i(\xi_{\mathbf{k}}^{(y)} + \xi_{-\mathbf{k}}^{(y)}))\omega_{\pm}(\mathbf{k}) \\ + (\Delta_{\mathbf{k}}^{(x)} + i(\Delta_{\mathbf{k}}^{(y)})^*)\{(\xi_{\mathbf{k}}^{(x)} + i\xi_{\mathbf{k}}^{(y)})(\xi_{-\mathbf{k}}^{(x)} - i\xi_{-\mathbf{k}}^{(y)})\} - (\Delta_{\mathbf{k}}^{(x)} - i\Delta_{\mathbf{k}}^{(y)})(\Delta_{\mathbf{k}}^{(x)} - i(\Delta_{\mathbf{k}}^{(y)})^*) \\ + (\Delta^{(0)})\left\{-\xi^{(0)}(\xi_{\mathbf{k}}^{(x)} + \xi_{-\mathbf{k}}^{(x)} + i(\xi_{\mathbf{k}}^{(y)} - \xi_{-\mathbf{k}}^{(y)})) + \Delta^{(0)}(\Delta_{\mathbf{k}}^{(x)} - i\Delta_{\mathbf{k}}^{(y)})\right\}, \quad (\text{B22})$$

$$\frac{V_{\pm,B}(\mathbf{k})}{(\Delta^{(0)})^2 - (\Delta_{\mathbf{k}}^{(x)})^2 + \{(\Delta_{\mathbf{k}}^{(y)})^*\}^2} = -(\xi^{(0)} + \omega_{\pm}(\mathbf{k}))(\xi_{\mathbf{k}}^{(x)} + i\xi_{\mathbf{k}}^{(y)})(\Delta_{\mathbf{k}}^{(x)} + i(\Delta_{\mathbf{k}}^{(y)})^*) \\ - (\xi^{(0)} - \omega_{\pm}(\mathbf{k}))(\xi_{-\mathbf{k}}^{(x)} + i\xi_{-\mathbf{k}}^{(y)})(\Delta_{\mathbf{k}}^{(x)} - i(\Delta_{\mathbf{k}}^{(y)})^*) \\ + \Delta^{(0)}\left\{(\xi^{(0)})^2 + (\xi_{\mathbf{k}}^{(x)} + i\xi_{\mathbf{k}}^{(y)})(\xi_{-\mathbf{k}}^{(x)} + i\xi_{-\mathbf{k}}^{(y)}) - (\Delta^{(0)})^2\right. \\ \left. + (\Delta_{\mathbf{k}}^{(x)})^2 + ((\Delta_{\mathbf{k}}^{(y)})^*)^2 - (\omega_{\pm}(\mathbf{k}))^2\right\}. \quad (\text{B23})$$

The normalized eigenvector $\mathbf{t}_{\pm}(\mathbf{k})$ can be written as

$$\mathbf{t}_{\pm}(\mathbf{k}) = \begin{pmatrix} u_{\pm,A}(\mathbf{k}) \\ u_{\pm,B}(\mathbf{k}) \\ v_{\pm,A}(\mathbf{k}) \\ v_{\pm,B}(\mathbf{k}) \end{pmatrix} = \begin{pmatrix} e^{i\rho_{\pm,1}(\mathbf{k})} \cosh \chi_{\pm}(\mathbf{k}) \cos \mu_{\pm}(\mathbf{k}) \\ e^{i\rho_{\pm,2}(\mathbf{k})} \cosh \chi_{\pm}(\mathbf{k}) \sin \mu_{\pm}(\mathbf{k}) \\ e^{i\rho_{\pm,3}(\mathbf{k})} \sinh \chi_{\pm}(\mathbf{k}) \cos \nu_{\pm}(\mathbf{k}) \\ e^{i\rho_{\pm,4}(\mathbf{k})} \sinh \chi_{\pm}(\mathbf{k}) \sin \nu_{\pm}(\mathbf{k}) \end{pmatrix} \quad (\text{B24})$$

where $\rho_{\pm,1}(\mathbf{k}), \dots, \rho_{\pm,4}(\mathbf{k}) \in \mathbb{R}$, $\mu_{\pm}(\mathbf{k}), \nu_{\pm}(\mathbf{k}) \in [0, \pi/2]$ and $\chi_{\pm}(\mathbf{k}) \geq 0$. These values satisfy

$$\tanh \chi_{\pm}(\mathbf{k}) = \frac{\sqrt{|V_{\pm,A}(\mathbf{k})|^2 + |V_{\pm,B}(\mathbf{k})|^2}}{\sqrt{|U_{\pm,A}(\mathbf{k})|^2 + |U_{\pm,B}(\mathbf{k})|^2}} \quad (\text{B25})$$

$$\tan \mu_{\pm}(\mathbf{k}) = \left| \frac{U_{\pm,B}(\mathbf{k})}{U_{\pm,A}(\mathbf{k})} \right| \quad \tan \nu_{\pm}(\mathbf{k}) = \left| \frac{V_{\pm,B}(\mathbf{k})}{V_{\pm,A}(\mathbf{k})} \right| \quad (\text{B26})$$

$$e^{i\rho_{\pm,1}(\mathbf{k})} = \frac{U_{\pm,A}(\mathbf{k})}{|U_{\pm,A}(\mathbf{k})|} \quad e^{i\rho_{\pm,2}(\mathbf{k})} = \frac{U_{\pm,B}(\mathbf{k})}{|U_{\pm,B}(\mathbf{k})|} \quad e^{i\rho_{\pm,3}(\mathbf{k})} = \frac{V_{\pm,A}(\mathbf{k})}{|V_{\pm,A}(\mathbf{k})|} \quad e^{i\rho_{\pm,4}(\mathbf{k})} = \frac{V_{\pm,B}(\mathbf{k})}{|V_{\pm,B}(\mathbf{k})|}. \quad (\text{B27})$$

In the case of $D_{\parallel} = 0$ and $\phi_{\perp} = 0$, we can get the simple expression of the magnon bands and the corresponding parameters of the eigenvectors as

$$\omega_1(\mathbf{k}) = \sqrt{(\xi^{(0)} + \xi_{\mathbf{k}}^{(x)})^2 - (\Delta^{(0)} + \Delta_{\mathbf{k}}^{(x)})^2} \quad (\text{B28})$$

$$\omega_2(\mathbf{k}) = \sqrt{(\xi^{(0)} - \xi_{\mathbf{k}}^{(x)})^2 - (\Delta^{(0)} - \Delta_{\mathbf{k}}^{(x)})^2} \quad (\text{B29})$$

$$\tanh\chi_1(\mathbf{k}) = \sqrt{\frac{\xi^{(0)} + \xi_{\mathbf{k}}^{(x)} - \omega_1(\mathbf{k})}{\xi^{(0)} + \xi_{\mathbf{k}}^{(x)} + \omega_1(\mathbf{k})}} \quad (B30)$$

$$\tanh\chi_2(\mathbf{k}) = \sqrt{\frac{\xi^{(0)} - \xi_{\mathbf{k}}^{(x)} - \omega_2(\mathbf{k})}{\xi^{(0)} - \xi_{\mathbf{k}}^{(x)} + \omega_2(\mathbf{k})}} \quad (B31)$$

$$\tan\mu_1(\mathbf{k}) = \tan\nu_1(\mathbf{k}) = \tan\mu_2(\mathbf{k}) = \tan\nu_2(\mathbf{k}) = 1 \quad (B32)$$

$$e^{i\rho_{1,1}(\mathbf{k})} = e^{i\rho_{1,2}(\mathbf{k})} = 1 \quad e^{i\rho_{1,3}(\mathbf{k})} = e^{i\rho_{1,4}(\mathbf{k})} = -\text{sgn}(\Delta^{(0)} + \Delta_{\mathbf{k}}^{(x)}) \quad (B33)$$

$$e^{i\rho_{2,1}(\mathbf{k})} = e^{i\rho_{2,3}(\mathbf{k})} = 1 \quad e^{i\rho_{2,2}(\mathbf{k})} = e^{i\rho_{2,4}(\mathbf{k})} = -1. \quad (B34)$$

The eigenvector of the edge modes is given by

$$\mathbf{t}_{\mu}(k_{\delta_1}) = (u_{\mu,A}^{(1)}(k_{\delta_1}), u_{\mu,B}^{(1)}(k_{\delta_1}), \dots, u_{\mu,A}^{(2L)}(k_{\delta_1}), u_{\mu,B}^{(2L)}(k_{\delta_1}), v_{\mu,A}^{(1)}(k_{\delta_1}), v_{\mu,B}^{(1)}(k_{\delta_1}), \dots, v_{\mu,A}^{(2L)}(k_{\delta_1}), v_{\mu,B}^{(2L)}(k_{\delta_1})), \quad (B35)$$

where $\mu = L, R$ denotes the left and right edge modes. The local density of states of the two edge modes are given by

$$d_{\mu}^{(j)}(k_{\delta_1}) = \sum_{\alpha=A,B} \left\{ |u_{\mu,\alpha}^{(j)}(k_{\delta_1})|^2 + |v_{\mu,\alpha}^{(j)}(k_{\delta_1})|^2 \right\}, \quad (B36)$$

where j is the site index along the δ_2 -direction.

Appendix C: Direction of the nonreciprocal propagation

Using Eq.(9) and the relation, $\mathbf{t}_{\pm}^{\dagger} \Sigma^z \mathbf{t}_{\pm}(\mathbf{k}) = 1$, the derivative of $\omega_{\pm}(\mathbf{k})$ with respect to \mathbf{k} is given as follows;

$$\begin{aligned} \nabla_{\mathbf{k}} \omega_{\pm}(\mathbf{k}) &= \nabla_{\mathbf{k}} [\mathbf{t}_{\pm}^{\dagger}(\mathbf{k}) H_{\text{BdG}}(\mathbf{k}) \mathbf{t}_{\pm}(\mathbf{k})] \\ &= \mathbf{t}_{\pm}^{\dagger}(\mathbf{k}) [\nabla_{\mathbf{k}} H_{\text{BdG}}(\mathbf{k})] \mathbf{t}_{\pm}(\mathbf{k}) + \omega_{\pm}(\mathbf{k}) \nabla_{\mathbf{k}} [\mathbf{t}_{\pm}^{\dagger}(\mathbf{k}) \Sigma^z \mathbf{t}_{\pm}(\mathbf{k})] \\ &= \mathbf{t}_{\pm}^{\dagger}(\mathbf{k}) [\nabla_{\mathbf{k}} H_{\text{BdG}}(\mathbf{k})] \mathbf{t}_{\pm}(\mathbf{k}). \end{aligned} \quad (C1)$$

In the case of $\phi_{\perp} = 0$, we find

$$\nabla_{\mathbf{k}} \omega_{\pm}(\mathbf{k})|_{\mathbf{k}=\mathbf{0}} = \pm \text{sgn}(\xi^{(0)} \xi_{\mathbf{0}}^{(x)} - \Delta^{(0)} \Delta_{\mathbf{0}}^{(x)}) \sqrt{2} D_{\parallel} S \sin\theta_{\parallel} (e_x \cos\phi_{\parallel} - e_y \sin\phi_{\parallel}). \quad (C2)$$

Thus, the two bands have velocities of different sign at Γ point, and D_{\parallel} pushes the minima of these bands in the opposite directions, making the bands nonreciprocal.

Appendix D: Development of the Berry curvature with magnetic field

We show in Fig.9 the field angle dependence of the Berry curvature. In the case of $\phi_{\perp} = 45^{\circ}$, the peak position shifts to the $-k_x$ direction along $k_y = 0$ line due to the in-plane component of the magnetic field, \mathbf{h}_{\parallel} . While in the case of $\phi_{\perp} = 89^{\circ}$, the peak position does not shift. This is because the in-plane component of the magnetic field, $|\mathbf{h}_{\parallel}| = hc \cos 89^{\circ}$, is very small.

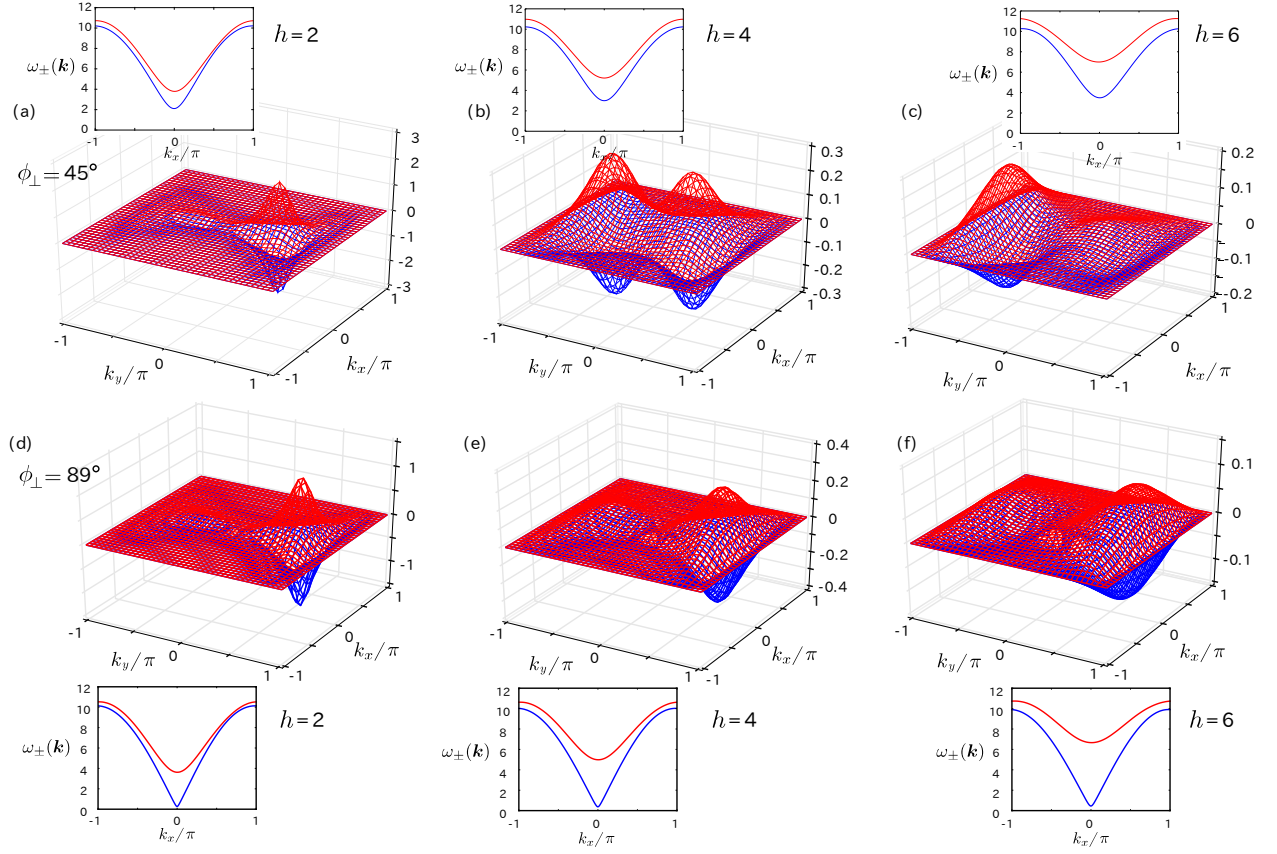


FIG. 9. Details of the Berry curvature $\Omega_{xy}^{(\pm)}(\mathbf{k})$ for field angles (a)-(c) $\phi_{\perp} = 45^\circ$ and (d)-(f) $\phi_{\perp} = 89^\circ$, with $h/J = 2, 4$, and 6 . The other parameters are taken as the same as Fig.4, $J = 1.0$, $D_{\parallel} = D_{\perp} = 0.2$, $\Lambda = 0.05$. When $\phi_{\perp} = 45^\circ$, the peak position shifts with increasing h in the $-k_x$ direction along $k_y = 0$. For $\phi_{\perp} = 89^\circ$, such peak-shift is not observed. The corresponding magnon bands along the $k_y = 0$ line are shown together.

¹ S. Murakami and A. Okamoto, J. Phys. Soc. Jpn. **86**, 011010 (2017).
² R. Cheng, S. Okamoto, and D. Xiao, Phys. Rev. Lett. **117**, 217202 (2016).
³ V. A. Zyuzin and A. A. Kovalev, Phys. Rev. Lett. **117**, 217203 (2016).
⁴ Y. Shiomi, R. Takashima, and E. Saitoh, Phys. Rev. B **96**, 134425 (2017).
⁵ H. Jin, S. R. Boona, Z. Yang, R. C. Myers, and J. P. Heremans, Phys. Rev. B **92**, 054436 (2015).
⁶ Y. Onose, T. Ideue, H. Katsura, Y. Shiomi, N. Nagaosa, and Y. Tokura, Science **329**, 297 (2010).
⁷ T. Ideue, Y. Onose, H. Katsura, Y. Shiomi, S. Ishiwata, N. Nagaosa, and Y. Tokura, Phys. Rev. B **85**, 134411 (2012).
⁸ H. Katsura, N. Nagaosa, P. A. Lee, Phys. Rev. Lett. **104**, 066403 (2010).
⁹ R. Matsumoto and S. Murakami, Phys. Rev. Lett. **106**, 197202 (2011).
¹⁰ R. Matsumoto and S. Murakami, Phys. Rev. B **84**, 184406 (2011).
¹¹ R. Matsumoto, R. Shindou, and S. Murakami, Phys. Rev. B **89**, 054420 (2014).
¹² S. A. Owerre, Phys. Rev. B **95**, 014422 (2017).
¹³ S. A. Owerre, J. Phys.: Condens. Matter **29**, 03LT01 (2017).
¹⁴ S. A. Owerre, J. Phys.: Condens. Matter **29**, 185801 (2017).
¹⁵ P. Laurell and G. A. Fiete, Phys. Rev. B **98**, 094419 (2018).
¹⁶ A. Mook, J. Henk, and I. Mertig, Phys. Rev. B **89**, 134409 (2014).
¹⁷ M. Hirschberger, R. Chisnell, Y. S. Lee, and N. P. Ong, Phys. Rev. Lett. **115**, 106603 (2015).
¹⁸ H. Lee, J. H. Han, and P. A. Lee, Phys. Rev. B **91**, 125413 (2015).
¹⁹ S. A. Owerre, Europhys. Lett. **117**, 37006 (2017).
²⁰ S. A. Owerre, J. Phys. Commun. **1**, 021001 (2017).
²¹ P. Laurell and G. A. Fiete, Phys. Rev. Lett. **118**, 177201 (2017).
²² S. A. Owerre, J. Phys.: Condens. Matter **28**, 47LT02 (2016).

²³ S. A. Owerre, *J. Phys.: Condens. Matter* **28**, 386001 (2016).

²⁴ S. A. Owerre, *Phys. Rev. B* **94**, 094405 (2016).

²⁵ S. A. Owerre, *J. Appl. Phys.* **120**, 043903 (2016).

²⁶ S. A. Owerre, *J. Phys. Commun.* **1**, 021002 (2017).

²⁷ S. A. Owerre, *J. Phys. Commun.* **1**, 025007 (2017).

²⁸ S. A. Owerre, *J. Phys.: Condens. Matter* **29**, 385801 (2017).

²⁹ S. A. Owerre, *J. Phys.: Condens. Matter* **29**, 455802 (2017).

³⁰ S. A. Owerre, *J. Appl. Phys.* **121**, 223904 (2017).

³¹ S. A. Owerre, arXiv:1802.04268 (2018).

³² K. Nakata, J. Klinovaja, and D. Loss, *Phys. Rev. B* **95**, 125429 (2017).

³³ K. Nakata, S. K. Kim, J. Klinovaja, and D. Loss, *Phys. Rev. B* **96**, 224414 (2017).

³⁴ K. A. van Hoogdalem, Y. Tserkovnyak, and D. Loss, *Phys. Rev. B* **87**, 024402 (2013).

³⁵ X. Cao, K. Chen, and D. He, *J. Phys.: Condens. Matter* **27**, 166003 (2017).

³⁶ S. Fujimoto, *Phys. Rev. Lett.* **103**, 047203 (2009).

³⁷ L. Zhang, J. Ren, J.-S. Wang, and B. Li, *Phys. Rev. B* **87**, 144101 (2013).

³⁸ A. Mook, J. Henk, and I. Mertig, *Phys. Rev. B* **90**, 024412 (2014).

³⁹ R. Chisnell, J. S. Helton, D. E. Freedman, D. K. Singh, R. I. Bewley, D. G. Nocera, and Y. S. Lee, *Phys. Rev. Lett.* **115**, 147201 (2015).

⁴⁰ A. Mook, J. Henk, and I. Mertig, *Phys. Rev. B* **91**, 174409 (2015).

⁴¹ A. Mook, J. Henk, and I. Mertig, *Phys. Rev. B* **91**, 224411 (2015).

⁴² A. Mook, J. Henk, and I. Mertig, *Phys. Rev. B* **94**, 174444 (2016).

⁴³ R. Seshadri and D. Sen, *Phys. Rev. B* **97**, 134411 (2018).

⁴⁴ F.-Y. Li, Y.-D. Li, Y. B. Kim, L. Balents, Y. Yu, and G. Chen, *Nat. Commun.* **7**, 12691 (2016).

⁴⁵ A. Mook, J. Henk, and I. Mertig, *Phys. Rev. Lett.* **117**, 157204 (2016).

⁴⁶ A. Mook, J. Henk, and I. Mertig, *Phys. Rev. B* **95**, 014418 (2017).

⁴⁷ Y. Su, X. S. Wang, and X. R. Wang, *Phys. Rev. B* **95**, 224403 (2017).

⁴⁸ S. K. Kim, H. Ochoa, R. Zarzuela, and Y. Tserkovnyak, *Phys. Rev. Lett.* **117**, 227201 (2016).

⁴⁹ X. S. Wang, Y. Su, and X. R. Wang, *Phys. Rev. B* **95**, 014435 (2017).

⁵⁰ S. A. Owerre, *Sci. Rep.* **7**, 6931 (2017).

⁵¹ P. A. Pantaleon and Y. Xian, *Physica B* **530**, 191 (2018).

⁵² S. A. Owerre, *Sci. Rep.* **8**, 4431 (2018).

⁵³ Y. Su and X. R. Wang, *Phys. Rev. B* **96**, 104437 (2017).

⁵⁴ X. S. Wang, H. W. Zhang, and X. R. Wang, *Phys. Rev. Appl.* **9**, 024029 (2018).

⁵⁵ I. Dzyaloshinsky, *J. Phys. Chem. Solids* **4**, 241-255 (1958).

⁵⁶ T. Moriya, *Phys. Rev.* **120**, 91 (1960).

⁵⁷ Only in specific cases, the cancellation of the effect of the U(1) gauge field is avoided, such as the system with spatial dependent electric field^{32,33} or having a nontrivial spin texture in real space³⁴.

⁵⁸ T. Jungwirth, Q. Niu, and A. H. MacDonald, *Phys. Rev. Lett.* **88**, 207208 (2002).

⁵⁹ M. Onoda, and N. Nagaosa, *J. Phys. Soc. Jpn.* **71**, 19 (2002).

⁶⁰ Z. Fang, N. Nagaosa, K. S. Takahashi, A. Asamitsu, R. Mathien, T. Ogasawara, H. Yamada, M. Kawasaki, Y. Tokura, and K. Terakura, *Science* **302**, 92 (2003).

⁶¹ D. Culcer, A. MacDonald, and Q. Niu, *Phys. Rev. B* **68**, 045327 (2003).

⁶² T. Jungwirth, J. Sinova, K. Y. Wang, K. W. Edmonds, R. P. Campion, B. L. Gallagher, C. T. Foxon, Q. Niu, and A. H. MacDonald, *Appl. Phys. Lett.* **83**, 320 (2003).

⁶³ D. Culcer, J. Sinova, N. A. Sinitsyn, T. Jungwirth, A. H. MacDonald, and Q. Niu, *Phys. Rev. Lett.* **93**, 046602 (2004).

⁶⁴ Y. Yao, L. Kleinman, A. H. MacDonald, J. Sinova, T. Jungwirth, D.-S. Wang, E. Wang, and Q. Niu, *Phys. Rev. Lett.* **92**, 037204 (2004).

⁶⁵ V. K. Dugaev, P. Bruno, M. Taillefumier, B. Canals, and C. Lacroix, *Phys. Rev. B* **71**, 224423 (2005).

⁶⁶ E. I. Rashba, *Fizika. tela* **2**, 1224 (1960) [Sov. Phys. Solid State **2**, 1109 (1960).]

⁶⁷ R. C. Casella *Phys. Rev. Lett.* **5**, 371 (1960).

⁶⁸ Y. A. Bychkov, and E. I. Rashba, *J. Phys. C* **17**, 6039 (1984).

⁶⁹ G. Dresselhaus, *Phys. Rev.* **100**, 580 (1955).

⁷⁰ N. Hatano, R. Shirasaki, and H. Nakamura, *Phys. Rev. A* **75**, 032107 (2007).

⁷¹ T. Masuda, S. Kitaoka, S. Takamizawa, N. Metoki, K. Kaneko, K. C. Rule, K. Kiefer, H. Manaka, and H. Nojiri, *Phys. Rev. B* **81**, 100402 (2010).

⁷² Y. Iguchi, Y. Nii, M. Kawano, H. Murakawa, N. Hanasaki, and Y. Onose, *Phys. Rev. B* **98**, 064416 (2018).

⁷³ H. Murakawa, Y. Onose, S. Miyahara, N. Furukawa, and Y. Tokura, *Phys. Rev. B* **85**, 174106 (2012).

⁷⁴ A. Zheludev, T. Sato, T. Masuda, K. Uchinokura, G. Shirane, and B. Roessli, *Phys. Rev. B* **68**, 024428 (2003).

⁷⁵ H. Murakawa, Y. Onose, S. Miyahara, N. Furukawa, and Y. Tokura, *Phys. Rev. Lett.* **105**, 137202 (2010).

⁷⁶ M. Kawano, Y. Onose, and C. Hotta, arXiv:1805.03925.

⁷⁷ M. E. Zhitomirsky and T. Nikuni, *Phys. Rev. B* **57**, 5013 (1998).

⁷⁸ T. Holstein and H. Primakoff, *Phys. Rev.* **58**, 1098 (1940).

⁷⁹ J. H. P. Colpa, *Physica* **93A**, 327 (1978).

⁸⁰ R. Shindou, R. Matsumoto, S. Murakami, and J. I. Ohe, *Phys. Rev. B* **87**, 174427 (2013).

⁸¹ M. Sato and S. Fujimoto, *Phys. Rev. B* **79**, 094504 (2009).

⁸² S. Sato and Y. Ando, *Rep. Prog. Phys.* **80**, 876501 (2017).

⁸³ K. Asano and C. Hotta, *Phys. Rev. B* **83**, 245125 (2011).

⁸⁴ Having a nonvanishing Berry curvature is necessary but not sufficient to realize topological edge modes. There are cases where the topologically protected edge mode is absent and the Chern number remains zero, even when the Berry curvature is finite⁸⁵.

⁸⁵ J. Romhanyi, K. Penc, and R. Ganesh, *Nat. Commun.* **6**, 6805 (2015).

⁸⁶ J.-i. Kishine and A. S. Ovchinnikov, *Solid State Physics* **66** (2015) 1-130.